Sparse Logistic Regression-Based One-Bit SAR Imaging

Shaodi Ge, Dong Feng, Shaoqiu Song, Jian Wang, and Xiaotao Huang, *Member, IEEE*

***Abstract*— One-bit synthetic aperture radar (SAR) imaging has garnered significant interest due to its ability to lower the cost of storing enormous amounts of data during sampling and transmission, as well as the expense of analog-to-digital converters (ADCs). However, existing one-bit SAR imaging methods suffer from high computational complexity and artifacts in the resulting images. To address these problems, the sparse logistic regression (SLR) model solved by iterative hard thresholding (IHT) is applied to one-bit SAR imaging, and a new SLR-IHT imaging method is proposed. The SLR-IHT method models the one-bit SAR imaging problem as an SLR task and optimizes the solution using the IHT framework. By leveraging the joint sparsity of the real and imaginary components, the proposed method enhances imaging quality while effectively suppressing artifacts. To accelerate computation, the Armijo step size criterion is employed to adjust the step size and support set during the iterative procedure. Moreover, a theoretical investigation into the convergence properties of the proposed method was conducted. Extensive simulations and real data experiments are conducted to evaluate the performance of the SLR-IHT method. The results demonstrate its superiority over existing one-bit SAR imaging techniques in terms of imaging quality and computational efficiency.**

***Index Terms*— Iterative hard thresholding (IHT), one-bit quantization, sparse logistic regression (SLR), synthetic aperture radar (SAR) imaging.**

I. Introduction

SYNTHETIC aperture radar (SAR) imaging systems offer the advantage of operating independently of time and weather conditions, making them widely utilized in both military and civilian applications [1], [2], [3], [4], [5], [6], [7], [8]. However, achieving fast and accurate analog-to-digital converter (ADC) requires expensive hardware enhancements. To address the challenges associated with storage and transmission, radar signal processing techniques utilizing one-bit sampled data have garnered considerable attention [9], [10], [11], [12], [13], [14], [15], [16], [17], [18], [19], [20]. One-bit sampling involves comparing the received signal with a reference quantization level and recording whether the signal is above or below this level [11], [12], [13]. As a result, the quantized measurements possess simple symbolic values. The significant advantage of one-bit quantization is its ability to support very high sampling rates while maintaining lower costs and energy consumption compared to conventional ADCs [21], [22].

Back in the 1990s, some researchers explored one-bit sampling quantization and imaging of SAR data, and they also developed real-time processing architecture designs and prototype implementations [22], [23], [24], [25]. These studies indicated that a low SNR could reduce the impact of nonlinear quantization caused by one-bit quantization. The imaging results of the one-bit matched filtering (MF) method did not exhibit significant degradation in imaging performance. Furthermore, doubling the oversampling frequency could reduce the overlap effects between fundamental and higher-order harmonics, resulting in imaging results very similar to those obtained with high-bit quantization in traditional MF imaging, albeit with an increase in sampled data volume [24]. However, in situations with relatively low SNR, there is often a higher level of noise, leading to a decrease in the performance of traditional MF and a corresponding decline in the performance of the one-bit MF method. As the SNR increased, the quantization effects of one-bit sampling exacerbated the nonlinear distortion of the signal spectrum, leading to an increase in higher-order harmonic components, spectral broadening, and significant impact on frequency components within the signal band. Consequently, the direct application of one-bit MF methods made it challenging to attain high-quality imaging results.

Given the prevalence of sparse scenes in SAR imaging, sparse imaging methods based on compressive sensing (CS) have garnered significant research interest. These methods enable high-resolution imaging of sparse scenes with only a small number of measurements [26], [27], [28], [29]. However, the CS imaging methods designed for precise data are not directly applicable to the echo data obtained from one-bit quantization. To address this issue, several one-bit CS methods have been proposed to tackle the signal recovery task with one-bit quantized data. In [30], the one-bit CS approach is employed for the first time to accomplish SAR sparse imaging using one-bit measurements. This method is based on the Bayesian maximum a posteriori estimation framework, which derives a mathematical model for reconstructing SAR images from one-bit measurements. The optimization problem is solved using a first-order primal-dual algorithm. Experimental results demonstrate that this method effectively mitigates false targets and enhances target-background contrast. In addressing the nonlinear distortion problem of one-bit sampling quantization, Jacques et al. [31] and Demir and Erçelebi [32] explore a time-varying threshold-based one-bit CS method to recover

Manuscript received 18 July 2023; revised 5 September 2023 and 2 October 2023; accepted 3 October 2023. Date of publication 6 October 2023; date of current version 18 October 2023. This work was supported in part by the National Science Foundation of China under Grant 62101566. *(Corresponding author: Dong Feng.)*

The authors are with the College of Electronic Science, National University of Defense Technology, Changsha 410073, China (e-mail: feng_dong_nudt@126.com).

Digital Object Identifier 10.1109/TGRS.2023.3322554

the amplitude information lost in nonlinear quantization. The one-bit model with time-varying thresholding is similar to the model with fixed zero thresholding and only requires a comparator to be implemented. However, for more precise signal estimation, the time-varying Gaussian thresholding strategy must record the threshold value at each moment. In [33], a binary CS with time-varying thresholds method (BCST) is proposed, eliminating the need for unit norm constraints or consistency functions between measurements and estimates. This method offers the advantage of solving the one-bit SAR sparse imaging problem without complex optimization techniques. It employs variable separation and the alternating direction method of multipliers (ADMM) to handle the optimization problem. However, using ADMM involves matrix inversion operations, resulting in high computational complexity. Moreover, the storage of time-varying thresholds still requires significant resources, limiting the full potential of one-bit quantization. In contrast, using a fixed non-zero threshold can achieve signal amplitude recovery but is limited to a small range of signal threshold ratios and performs less effectively than the random Gaussian threshold method [11].

The binary iterative hard thresholding (BIHT) method addresses quantization errors by enforcing consistent reconstruction, which has the advantage of easy implementation and has been demonstrated to be successful and efficient in enhancing the performance of one-bit signal recovery [31], [34], [35]. Building upon this foundation, several researchers have proposed one-bit SAR imaging approaches based on the BIHT method framework [10], [36], [37]. In [36], an adaptive BIHT (A-BIHT) method is proposed, which introduces an adaptive quantization level parameter scheme and iteratively updates the imaging results and quantization level parameters. Moreover, the presence of noise in the echo data can lead to erroneous one-bit measurements, affecting the consistency of reconstruction conditions and resulting in artifacts in the final imaging results. By updating the quantization level parameters in each iteration, the A-BIHT method relaxes the quantization consistency constraint to accommodate certain inconsistencies introduced by noise. Wang et al. [10] argue that existing one-bit CS SAR imaging methods should take into account the clustering and joint sparse characteristics commonly observed in radar backscattering applications. Clustering refers to the spatial range of the target being imaged, where the majority of targets extend to a group of adjacent pixels. The clustering structure of the target image can be exploited to eliminate isolated artifacts [38], [39]. The joint sparse pattern describes the similarity in structure between the real and imaginary parts of the data samples, with both parts largely sharing zero or non-zero values simultaneously [40]. Based on this insight, an enhanced BIHT (E-BIHT) method is proposed, resulting in an image with a higher target clutter ratio. Motivated by the advantages of adversarial samples, Han et al. [37] introduce the adversarial sample-based BIHT (AS-BIHT) method for one-bit radar CS imaging. AS-BIHT formulates the one-bit radar imaging problem by constructing a quantized level parameter within the imaging process and defining the problem as a one-bit radar imaging problem with a quantized level parameter as a parametric model. The parameterized one-bit radar imaging model leverages adversarial samples to train quantization level parameters, thereby improving one-bit imaging performance. The quantization level parameters are adaptively adjusted by seeking quantization-consistent solutions on the updated imaging scene and related adversarial samples in each iteration. This method reduces quantization inconsistencies arising from one-bit quantization and noise, resulting in the elimination of artifacts. Experimental results demonstrate that the AS-BIHT method outperforms conventional one-bit CS techniques in one-bit radar imaging performance.

In the aforementioned one-bit SAR CS imaging methods, regardless of whether they are based on the BIHT framework or ADMM method [10], [33], [36], [37], a significant number of matrix-vector multiplication or matrix inversion operations are inevitably required. Particularly for large-scale one-bit SAR imaging applications, such computations are time-consuming, and the imaging results are still affected by artifacts. To tackle these challenges, this article adopts a perspective of sparse logistic regression (SLR) for one-bit CS imaging. It treats the problem as the estimation of parameter vectors (i.e., reflection coefficients) given samples (i.e., observation matrix in CS theory) and labels (i.e., one-bit measurements). SLR represents a classic logistic regression model with sparse constraints, which has demonstrated effectiveness in various fields such as neural networks, deep learning, and bioinformatics for tasks like classification and feature selection [41], [42], [43], [44], [45]. Therefore, this article formulates the problem of one-bit SAR imaging as an SLR optimization problem, leveraging the nonlinear differentiable logistic function for learning and representing nonlinear patterns as a favorable substitute for the sign$(\cdot)$ function [46], [47]. To address the proposed optimization problem, we introduce the iterative hard thresholding (IHT) framework and propose a novel SLR-IHT method for one-bit imaging. During the iterative process, the Armijo line search step is utilized to adjust the step size and support set automatically, thereby expediting the computational speed. By imposing joint sparsity constraints on both the real and imaginary parts, the imaging quality is improved, leading to a reduction in the impact of artifacts. Furthermore, a theoretical analysis of the convergence behavior of the proposed optimization method has been conducted, confirming that the optimization approach consistently drives the objective function to diminish as the number of iterations increases. Finally, extensive simulations and real data experiments demonstrate that the proposed method achieves effective imaging in sparse scenes with only a small amount of data. It outperforms existing state-of-the-art one-bit imaging methods in terms of computational efficiency and imaging quality.

The remainder of the article is structured as follows: Section II introduces the one-bit SAR imaging signal model. Section III describes the suggested one-bit SAR imaging methods in detail and theoretically analyzed. In Section IV, the effectiveness of the proposed method is validated through extensive simulations and real radar data, with quantitative evaluation and analysis of the experimental results. In Section V, a conclusion is provided.

II. One-Bit SAR Imaging Model

Consider a SAR imaging model with a stepped-frequency waveform, where the radar emits multiple pulse sequences while in motion. The radar data is the superposition of echoes from all scatterers in the illuminated region by the radar beam. Assuming the scatterers in the scene are stationary, the stepped-frequency radar system consists of M available pulse sequences and N available frequencies for each sequence. The received signal for the nth pulse in the mth sequence can be represented as follows:

$$\widetilde{y}(m,n)=\iint_{\mathbf{G}}\widetilde{\Theta}(x,y)\cdot\exp\left[-j2\pi f_n\tau(m,n,x,y)\right]\mathrm{d}x\mathrm{d}y \tag{1}$$

where f_n denote the nth pulse frequency, (x,y) are the coordinates of the target, $\widetilde{\Theta}(x,y)$ is the reflection coefficient of the target at (x,y), $\tau(m,n,x,y)$ represents the time delay of the target at (x,y), and $\mathbf{G}$ denotes the area illuminated by the radar beam. In order to describe the radar data in the discrete space domain, the scene needs to be discretized. It is commonly assumed that the scene consists of a set of point scatterers distributed on a grid, with the grid points representing the locations of the scatterers. The reflection coefficients of the scatterers can be represented as a 2-D matrix denoted by

$$\mathbf{G}=\begin{bmatrix}\widetilde{\Theta}(1,1) & \cdots & \widetilde{\Theta}(1,Q)\\ \vdots & \ddots & \vdots\\ \widetilde{\Theta}(P,1) & \cdots & \widetilde{\Theta}(P,Q)\end{bmatrix} \tag{2}$$

where P is the number of points along the x-axis and Q is the number of points along the y-axis after scene discretization. To represent the radar data in matrix multiplicative form, the 2-D reflection coefficient matrix needs to be reshaped into a column vector $\widetilde{\mathbf{\Theta}}=[\widetilde{\Theta}(1,1),\ldots,\widetilde{\Theta}(P,1),\ldots,\widetilde{\Theta}(1,Q),\ldots,\widetilde{\Theta}(P,Q)]^T$, where $\widetilde{\mathbf{\Theta}}$ is a $PQ\times 1$ vector. Based on (2), the discrete expression of the radar echo data is obtained as

$$\widetilde{y}(m,n)=\sum_{i=1}^{PQ}\widetilde{\Theta}_i\cdot\exp\left[-j2\pi f_n\tau(m,n,i)\right] \tag{3}$$

where PQ represents the total number of targets after discretizing the scene, $\widetilde{\Theta}_i$ denotes the reflection coefficient of the ith target (i.e., the ith element in $\widetilde{\mathbf{\Theta}}$), and $\tau(m,n,i)$ represents the time delay of the ith target. Equation (3) can be expressed in matrix form as

$$\widetilde{\mathbf{y}}=\widetilde{\mathbf{\Phi}}\widetilde{\mathbf{\Theta}}+\widetilde{\mathbf{w}} \tag{4}$$

where $\widetilde{\mathbf{y}}=[\widetilde{\mathbf{y}}_1,\widetilde{\mathbf{y}}_2,\ldots,\widetilde{\mathbf{y}}_M]^T\in\mathbb{C}^{MN\times 1}$ is the measurement vector, and $\widetilde{\mathbf{y}}_m=[y_{m,1},y_{m,2},\ldots,y_{m,N}]\in\mathbb{C}^{1\times N}$, $\widetilde{\mathbf{w}}\in\mathbb{C}^{MN\times 1}$ is the additive noise vector. $\widetilde{\mathbf{\Phi}}=[\widetilde{\mathbf{\Phi}}_1^T,\widetilde{\mathbf{\Phi}}_2^T\cdots\widetilde{\mathbf{\Phi}}_M^T]^T$ is called the observation matrix and

$$\widetilde{\mathbf{\Phi}}_m=\exp\left(-j2\pi\mathbf{f}_m\otimes\tau_m^T\right)\in\mathbb{C}^{N\times PQ},\quad m=1,2,\ldots,M \tag{5}$$

where $\mathbf{f}_m=[f_1,f_2,\ldots,f_N]^T$ and $\tau_m=[\tau(m,1),\tau(m,i),\ldots,\tau(m,PQ)]^T$ represent the frequency and time delay vectors of the mth pulse sequence, respectively. The symbol $\otimes$ denotes the Kronecker product. Since the received measurements are recorded and quantized separately on the I and Q channels, the real and imaginary parts of (4) are separated, i.e.,

$$\mathbf{y}=\begin{bmatrix}\mathrm{Re}(\widetilde{\mathbf{y}})\\ \mathrm{Im}(\widetilde{\mathbf{y}})\end{bmatrix},\quad \mathbf{\Phi}=\begin{bmatrix}\mathrm{Re}\left(\widetilde{\mathbf{\Phi}}\right) & -\mathrm{Im}\left(\widetilde{\mathbf{\Phi}}\right)\\ \mathrm{Im}\left(\widetilde{\mathbf{\Phi}}\right) & \mathrm{Re}\left(\widetilde{\mathbf{\Phi}}\right)\end{bmatrix}$$
$$\mathbf{\Theta}=\begin{bmatrix}\mathrm{Re}\left(\widetilde{\mathbf{\Theta}}\right)\\ \mathrm{Im}\left(\widetilde{\mathbf{\Theta}}\right)\end{bmatrix},\quad \mathbf{w}=\begin{bmatrix}\mathrm{Re}(\widetilde{\mathbf{w}})\\ \mathrm{Im}(\widetilde{\mathbf{w}})\end{bmatrix} \tag{6}$$

where $\mathrm{Re}(\cdot)$ and $\mathrm{Im}(\cdot)$ denote the real and imaginary parts, respectively, and (4) is reformulated as

$$\mathbf{y}=\mathbf{\Phi\Theta}+\mathbf{w}. \tag{7}$$

The quantization threshold vector in a one-bit SAR imaging system can be expressed as $\lambda\in\mathbb{R}^{2MN\times 1}$, and the one-bit measurement vector can be obtained as

$$\mathbf{z}=\mathrm{sign}(\mathbf{y}-\lambda) \tag{8}$$

where $\mathrm{sign}(\cdot)$ is an element-by-element function, defined as

$$\mathrm{sign}(z)=\begin{cases}1, & \text{if } z\geq 0\\ -1, & \text{if } z<0.\end{cases} \tag{9}$$

To reduce the complexity of the imaging system, we adopt zero threshold quantization, represented by setting $\lambda=0$.

In many SAR imaging scenarios, the scene of interest is inherently sparse [26], [27], [28], i.e., only a few coefficients in $\mathbf{\Theta}$ are significantly non-zero, while the remaining coefficients are either zero or close to zero. Assume that the sparsity level of $\mathbf{\Theta}$ is $2K$, meaning that the number of dominant coefficients cannot exceed $2K$. Consequently, one-bit SAR imaging problem can be reformulated as the following optimization problem:

$$\begin{aligned}\widehat{\mathbf{\Theta}}&=\arg\min_{\mathbf{\Theta}}\|\mathbf{z}-\mathrm{sign}(\mathbf{\Phi\Theta})\|_0\\ &\text{s.t. }\|\mathbf{\Theta}\|_0\leq 2K,\quad \|\mathbf{\Theta}\|_2=1\end{aligned} \tag{10}$$

where the ℓ_2-norm constraint of $\|\mathbf{\Theta}\|_2=1$ is incorporated to prevent trivial all-zero solutions and ensure the uniqueness of the solution. One-bit SAR imaging aims to estimate $\mathbf{\Theta}$ based on the one-bit measurement vector $\mathbf{z}$. Since $\mathbf{\Theta}$ is a sparse signal, the one-bit CS techniques can be employed to solve the imaging problem.

Recent one-bit SAR imaging methods described in [10], [36], and [37] are modeled on the BIHT framework and are mainly reconstructed by constraining $\mathbf{\Theta}$ to be consistent with the one-bit measurement $\mathbf{z}$, denoted as

$$\begin{aligned}\widehat{\mathbf{\Theta}}&=\arg\min_{\mathbf{\Theta}}\|[\mathbf{z}\odot(\mathbf{\Phi\Theta})]_-\|_1\\ &\text{s.t. }\|\mathbf{\Theta}\|_0\leq 2K,\quad \|\mathbf{\Theta}\|_2=1\end{aligned} \tag{11}$$

where $[\cdot]_-$ denotes a negative function, if $u_i<0$, $[u_i]_-=u_i$, otherwise $[u_i]_-=0$. The symbol $\odot$ stands for Hadamard product. Specifically, during the kth iteration, given the initial

estimate $\boldsymbol{\Theta}$ and the one-bit measurement $\mathbf{z}$, the subgradient is calculated as follows:

$$\nabla \mathcal{J} = \boldsymbol{\Phi}^T\left(\mathbf{z} - \operatorname{sign}\left(\boldsymbol{\Phi}\boldsymbol{\Theta}^k\right)\right). \tag{12}$$

The iterative update formulas are obtained

$$\mathbf{a}^{k+1} = \boldsymbol{\Theta}^k - \alpha \nabla \mathcal{J} \tag{13}$$

$$\boldsymbol{\Theta}^{k+1} = \eta_{2K}\left(\mathbf{a}^{k+1}\right) \tag{14}$$

where α is a scalar that controls the gradient descent step, and $\eta_{2K}(\cdot)$ is a function that uses thresholding to find the optimal $2K$-term approximation of $\mathbf{a}$.

III. Proposed Methods

In contrast to previous one-bit SAR imaging techniques based on the BIHT framework, we model the one-bit measurements from the SLR perspective. SLR is a special nonlinear regression model with broad applicability in neural networks [48], [49], machine learning [50], bioinformatics [51], and other fields, demonstrating significant feature selection and classification abilities. Due to the prevalence and utility of SLR, various generalized techniques and models have been developed [52], [53], [54]. On this basis, this article transforms the one-bit CS imaging problem into an SLR optimization problem.

A. Sparse Logistic Regression

The observation model for SAR in the real number domain is described by (7). In order to accurately reconstruct the reflection coefficient $\boldsymbol{\Theta}$ of the target from binary echo data, the one-bit SAR imaging process involves estimating the parameter vector $\boldsymbol{\Theta}$ given the samples $\boldsymbol{\Phi}$ and labels $\mathbf{z}$. Traditional logistic regression models are commonly employed when the number of samples exceeds the number of features. However, in many practical applications, this model may suffer from underdetermination issues, leading to overfitting problems. For instance, in data mining and machine learning, only a few features are typically crucial, making sparse criteria for input features desirable for faster prediction or better pattern interpretation. By imposing sparse constraints, the number of features can be reduced to effectively capture the characteristics of real-world problems, resulting in the widely studied SLR problem. Since targets with high scattering coefficients often exhibit a sparse distribution [26], [27], [28], the one-bit SAR sparse imaging problem can be naturally formulated as an SLR problem. For one-bit quantized data $\mathbf{z} \in \{1, -1\}$, the following probabilistic model is assumed:

$$\mathbb{P}\left(z_i = \pm 1 \mid \boldsymbol{\Phi}_{i,:}\right) = \frac{1}{1 + \exp\left(-z_i\left(\boldsymbol{\Phi}_{i,:}\boldsymbol{\Theta}\right)\right)} \tag{15}$$

where $\boldsymbol{\Phi}_{i,:}$ represents the ith row of $\boldsymbol{\Phi}$, $i = 1, 2, \ldots, 2MN$, $\mathbb{P}(z_i)$ denotes the conditional probability of label z_i given the sample $\boldsymbol{\Phi}_{i,:}$ and the parameter vector $\boldsymbol{\Theta}$. $\mathbb{P}(z_i = 1 \mid \boldsymbol{\Phi}_{i,:}) + \mathbb{P}(z_i = -1 \mid \boldsymbol{\Phi}_{i,:}) = 1$. If $(\boldsymbol{\Phi}_{i,:}\boldsymbol{\Theta}) \to +\infty$

$$\begin{cases} \lim\limits_{(\boldsymbol{\Phi}_{i,:}\boldsymbol{\Theta})\to+\infty} \mathbb{P}\left(z_i = 1 \mid \boldsymbol{\Phi}_{i,:}\right) = \dfrac{1}{1 + \exp\left(-z_i\left(\boldsymbol{\Phi}_{i,:}\boldsymbol{\Theta}\right)\right)} = 1 \\ \lim\limits_{(\boldsymbol{\Phi}_{i,:}\boldsymbol{\Theta})\to+\infty} \mathbb{P}\left(z_i = -1 \mid \boldsymbol{\Phi}_{i,:}\right) = \dfrac{1}{1 + \exp\left(-z_i\left(\boldsymbol{\Phi}_{i,:}\boldsymbol{\Theta}\right)\right)} = 0 \end{cases}$$

if $(\boldsymbol{\Phi}_{i,:}\boldsymbol{\Theta}) \to -\infty$

$$\begin{cases} \lim\limits_{(\boldsymbol{\Phi}_{i,:}\boldsymbol{\Theta})\to-\infty} \mathbb{P}\left(z_i = 1 \mid \boldsymbol{\Phi}_{i,:}\right) = \dfrac{1}{1 + \exp\left(-z_i\left(\boldsymbol{\Phi}_{i,:}\boldsymbol{\Theta}\right)\right)} = 0 \\ \lim\limits_{(\boldsymbol{\Phi}_{i,:}\boldsymbol{\Theta})\to-\infty} \mathbb{P}\left(z_i = -1 \mid \boldsymbol{\Phi}_{i,:}\right) = \dfrac{1}{1 + \exp\left(-z_i\left(\boldsymbol{\Phi}_{i,:}\boldsymbol{\Theta}\right)\right)} = 1. \end{cases}$$

Therefore, (15) can be seen as utilizing the logistic function $\sigma(z_i(\boldsymbol{\Phi}_{i,:}\boldsymbol{\Theta})) = 1/(1 + \exp(-z_i(\boldsymbol{\Phi}_{i,:}\boldsymbol{\Theta})))$ to quantify the consistency between the measurement value z_i and the estimated value $\boldsymbol{\Phi}_{i,:}\boldsymbol{\Theta}$. When $\boldsymbol{\Phi}_{i,:}\boldsymbol{\Theta}$ is larger, the probability of $z_i = 1$ is higher, and when $\boldsymbol{\Phi}_{i,:}\boldsymbol{\Theta}$ is smaller, the probability of $z_i = -1$ is higher. Hence, it effectively models the accuracy of one-bit quantization. To estimate the weight parameter $\boldsymbol{\Theta}$ using $2MN$ independent and identically distributed samples $(\boldsymbol{\Phi}_{i,:}, z_i)$, $i = 1, 2, \ldots, 2MN$, the classical logistic regression model can be obtained by solving the maximum likelihood estimation

$$\begin{aligned} L(\boldsymbol{\Theta}) &= \prod_{i=1}^{2MN} \mathbb{P}\left(\mathbf{z} = z_i \mid \boldsymbol{\Phi} = \boldsymbol{\Phi}_{i,:}\right) \\ &= \prod_{i=1}^{2MN} \sqrt{\mathbb{P}\left(\boldsymbol{\Phi}_{i,:}\right)^{1+z_i}\left(1 - \mathbb{P}\left(\boldsymbol{\Phi}_{i,:}\right)\right)^{(1-z_i)}}. \end{aligned} \tag{16}$$

Taking the logarithm of (16), we can get

$$\begin{aligned} \log(L(\boldsymbol{\Theta})) = \sum_{i=1}^{2MN} \Bigg[&-\frac{1}{2}(1 + z_i)\log\left(1 + \exp\left(-\left(\boldsymbol{\Phi}_{i,:}\boldsymbol{\Theta}\right)\right)\right) \\ &-\frac{1}{2}(1 - z_i)\log\left(1 + \exp\left(\boldsymbol{\Phi}_{i,:}\boldsymbol{\Theta}\right)\right)\Bigg] \end{aligned} \tag{17}$$

and

$$\begin{cases} -\dfrac{1}{2}(1 + z_i)\log(1 + \exp-(\boldsymbol{\Phi}_{i,:}\boldsymbol{\Theta})) \\ \qquad = -\log(1 + \exp(-(\boldsymbol{\Phi}_{i,:}\boldsymbol{\Theta}))), \quad \text{if } z_i = +1 \\ -\dfrac{1}{2}(1 - z_i)\log(1 + \exp(\boldsymbol{\Phi}_{i,:}\boldsymbol{\Theta})) \\ \qquad = -\log(1 + \exp(\boldsymbol{\Phi}_{i,:}\boldsymbol{\Theta})), \quad \text{if } z_i = -1. \end{cases} \tag{18}$$

By introducing both the l_0 sparsity constraint and the l_2 norm constraint, and assuming that the maximum number of non-zero elements in $\boldsymbol{\Theta}$ does not exceed $2K$, we define the following sparse optimization problem:

$$\begin{aligned} &\arg\min_{\boldsymbol{\Theta}} f(\boldsymbol{\Theta}) = \sum_{i=1}^{2MN} \log\left(1 + \exp\left(-z_i\left(\boldsymbol{\Phi}_{i,:}\boldsymbol{\Theta}\right)\right)\right) \\ &\text{s.t. } \| \boldsymbol{\Theta} \|_0 \le 2K, \| \boldsymbol{\Theta} \|_2 = 1. \end{aligned} \tag{19}$$

Given that the real and imaginary parts of the complex reflection coefficient vector $\boldsymbol{\Theta}$ can be viewed as projections onto two orthogonal axes, it is observed that they often exhibit similar structures. Specifically, the real and imaginary parts of $\boldsymbol{\Theta}$ tend to exhibit consistency in terms of assuming zero or non-zero values, indicating a joint sparse pattern. By incorporating this joint sparsity constraint into (19), the objective function can

be expressed as follows:

$$\arg\min_{\mathbf{\Theta}} f(\mathbf{\Theta}) = \sum_{i=1}^{2MN} \log\left(1+\exp\left(-z_i\left(\mathbf{\Phi}_{i,:}\mathbf{\Theta}\right)\right)\right)$$
$$\text{s.t.} \sum_{i=1}^{PQ} \| \sqrt{(\mathbf{\Theta}_i)^2 + \left(\mathbf{\Theta}_{i+PQ}\right)^2} \|_0 \le K, \| \mathbf{\Theta} \|_2 = 1. \quad (20)$$

Thus, the one-bit imaging problem is turned into the solution model (20).

B. Optimization Method

The IHT method has gained significant attention due to its simple implementation and favorable recovery characteristics. Thus, we employ the IHT framework along with the Armijo-type step size criterion to autonomously adjust the step size and support set for solving optimization problem (20). The parameter vector $\mathbf{\Theta}$ is iteratively updated according to the following three main steps.

1) Gradient Descent and Debiasing: The gradient descent step is calculated as

$$h(\mathbf{\Theta}) = (\mathbf{\Theta} - \alpha \nabla f(\mathbf{\Theta})) \quad (21)$$

where α represents the step size and $\nabla f(\mathbf{\Theta})$ denotes the gradient of (20), that is,

$$\nabla f(\mathbf{\Theta}) = -\mathbf{\Phi}^T \mathbf{z} \odot \frac{\exp(-\mathbf{z} \odot (\mathbf{\Phi}\mathbf{\Theta}))}{1+\exp(-\mathbf{z} \odot (\mathbf{\Phi}\mathbf{\Theta}))}. \quad (22)$$

Choose T_K as the optimal support of size $2K$ for $h(\mathbf{\Theta})$. Specifically, T_K comprises a set of indices that correspond to the maximum $2K$ absolute elements in $h(\mathbf{\Theta})$

$$\mathbf{\Theta}_{T_K} = \eta_{2K}(h(\mathbf{\Theta})). \quad (23)$$

Once T_K is selected, the debiasing step attempts to provide a better estimate by solving an optimization problem in a restricted subspace that is set to zero by setting all elements of $\mathbf{\Theta}$ with index T_K^C, where T_K^C is the complement of T_K in $\{1, 2, \ldots, 2PQ\}$ [41].

2) Armijo Line Search: During the gradient descent process, we employ the classical Armijo line search step size criterion to estimate the parameter α in (21). The Armijo criterion is guided by two key principles: the objective function value should be sufficiently minimized, and the line search step size should not be too small. Assuming that the estimated $\mathbf{\Theta}^k$ of $\mathbf{\Theta}$ is obtained during the kth iteration. Then, $\mathbf{\Theta}^k_{\alpha_l} = \eta_{2K}(\mathbf{\Theta}^k - \alpha_l \nabla f(\mathbf{\Theta}^k))$ is computed by iteration, where $\alpha_0 = \sqrt{k}$, $\alpha_l = \alpha_0 \beta^l$, and l is the smallest non-negative integer satisfying the following conditions:

$$f\left(\mathbf{\Theta}^k_{\alpha_l}\right) \le f\left(\mathbf{\Theta}^k\right) - \frac{\sigma}{2}\left|\left|\mathbf{\Theta}^k_{\alpha_l} - \mathbf{\Theta}^k\right|\right|^2 \quad (24)$$

where the parameter $(\sigma/2)$ is commonly selected as a tiny positive value. In Algorithm 1, we summarize the Armijo line search procedures.

After the debiasing step $\mathbf{\Theta}^k_{\alpha_l} = \eta_{2K}(\mathbf{\Theta}^k - \alpha_l \nabla f(\mathbf{\Theta}^k))$, it guarantees that the number of non-zero elements in $\mathbf{\Theta}^k_{\alpha_l}$ does not exceed $2K$ at each iteration. Hence, the computation of $\nabla f(\mathbf{\Theta})$, $f(\mathbf{\Theta}^k_{\alpha_l})$, and $f(\mathbf{\Theta}^k)$ can be sped up by constraining $\mathbf{\Phi}$, $\mathbf{\Theta}^k$ to its support set T_K, i.e.,

$$f(\mathbf{\Theta}) = \sum_{i=1}^{2MN} \log\left(1+\exp\left(-z_i\left(\left(\mathbf{\Phi}_{i,:}\right)_{T_K}\mathbf{\Theta}_{T_K}\right)\right)\right) \quad (25)$$

$$\nabla f(\mathbf{\Theta}) = -\mathbf{\Phi}^T \mathbf{z} \odot \frac{\exp\left(-\mathbf{z} \odot \left(\mathbf{\Phi}_{T_K}\mathbf{\Theta}_{T_K}\right)\right)}{1+\exp\left(-\mathbf{z} \odot \left(\mathbf{\Phi}_{T_K}\mathbf{\Theta}_{T_K}\right)\right)}. \quad (26)$$

The label subscript indicates that $\mathbf{\Phi}_{i,:}$ and $\mathbf{\Theta}$ only include elements which index belongs to T_K. Since the number of non-zero elements is significantly fewer than the number of pixels, i.e., $2K \ll 2PQ$, (25) and (26) can effectively reduce the computational complexity of the Armijo line search.

3) Joint Sparse Pattern: Due to the joint sparsity constraint in (20) being non-differentiable, for the $\mathbf{\Theta}^k_{\alpha_l}$ obtained by the Armijo line search, the greedy selection rule $\Gamma(\mathbf{\Theta}^k_{\alpha_l}, K)$ is used to guarantee the joint sparse pattern [10]. Definition $\Gamma(\mathbf{\Theta}, K)$ is an element-by-element operation, and $\Gamma(\Theta_i, K)$ is calculated as follows:

$$\Gamma(\Theta_i, K) = \begin{cases} \Theta_i, & \sqrt{(\Theta_i)^2 + \left(\Theta_{i+PQ}\right)^2} \ge \delta \\ 0, & \sqrt{(\Theta_i)^2 + \left(\Theta_{i+PQ}\right)^2} < \delta \end{cases} \quad i \le PQ \quad (27)$$

otherwise

$$\Gamma(\Theta_i, K) = \begin{cases} \Theta_i, & \sqrt{(\Theta_i)^2 + \left(\Theta_{i-PQ}\right)^2} \ge \delta \\ 0, & \sqrt{(\Theta_i)^2 + \left(\Theta_{i-PQ}\right)^2} < \delta \end{cases} \quad i > PQ. \quad (28)$$

In (27) and (28), δ is the Kth largest element of $\{((\Theta_i)^2 + (\Theta_{i+PQ})^2)^{1/2} \mid i = 1, 2, \ldots, PQ\}$.

At the kth iteration, the iteration stops wherever the maximum number of iterations $k_{\max}$ has been achieved or $|f(\mathbf{\Theta}^{k+1}) - f(\mathbf{\Theta}^k)| < 10^{-6}(1+|f(\mathbf{\Theta}^k)|)$ is satisfied. We summarize the proposed SLR-IHT method in Algorithm 2.

Remark 1: The selection of sparsity level K. Similar to existing one-bit CS imaging methods based on the BIHT framework [10], [36], [37], the proposed method is a greedy selection approach that requires specifying the sparsity level K as an input parameter. In the context of greedy algorithms, the selection of the sparsity parameter K can be based on empirical knowledge or involve running the method with a range of different sparsity levels K and subsequently choosing the most suitable sparse recovery result, albeit at the cost of increased

Algorithm 1 Armijo line search.

1) Input: $\mathbf{\Theta}^k$, $\nabla f(\mathbf{\Theta}^k)$, $\alpha_0 = \sqrt{k}$, β, σ, and maximum number of iterations l_{max};
2) Repeat the following, $l = 0, 1, 2, \ldots, l_{max}$
$\mathbf{\Theta}^k_{\alpha_l} = \eta_{2K}(\mathbf{\Theta}^k - \alpha_l \nabla f(\mathbf{\Theta}^k))$;
3) Until Eq. (24) is satisfied, or the maximum number of iterations is reached;
4) Output: $\mathbf{\Theta}^k_{\alpha_l}$.

Algorithm 2 SLR-IHT.

1) Input: The one-bit measurement vector $\mathbf{z}$, the observation matrix $\mathbf{\Phi}$, the sparsity level K, and the maximum number of iterations $k_{\max}$;
2) Initialization: $\mathbf{\Theta}^0 = \mathbf{0}$;
3) Repeat the following, $k = 0, 1, 2, \ldots, k_{max}$
a) Calculate the gradient $\nabla f(\mathbf{\Theta}^k)$;
b) Estimate $\mathbf{\Theta}^k_{\alpha_l}$ using Algorithm 1;
c) Joint sparse constraint $\mathbf{\Theta}^{k+1} = \Gamma(\mathbf{\Theta}^k_{\alpha_l}, K)$;
4) Until the iteration termination conditions are satisfied;
5) Output: Estimated value $\widehat{\mathbf{\Theta}} = \mathbf{\Theta}^{k+1}/\| \mathbf{\Theta}^{k+1} \|_2$.

computational complexity [10], [36]. Another strategy involves estimating the sparsity level K of the scene roughly based on MF theory by imaging the scene and analyzing the recovered image [55]. In Section IV, we perform an analysis of the proposed method's performance for various sparsity levels K using both simulated and real data. The results demonstrate that the proposed method consistently achieves better imaging results across a wide range of sparsity levels.

Remark 2: The selection of the observation matrix and its scalability. The SLR-IHT method is a sparsity-driven algorithm that achieves one-bit CS imaging with a small number of randomly selected echo samples. Assuming we randomly select M_r sequences from a total of M sequences, with N_r randomly selected frequency points per sequence, we can construct a new observation matrix $\mathbf{\Phi}' \in \mathbb{R}^{2M_rN_r \times 2PQ}$. Hence, the reduced measurement vector can be represented as

$$\mathbf{z}_r = \operatorname{sign}\left(\mathbf{\Phi}'\mathbf{\Theta} + \mathbf{w}_r\right) \tag{29}$$

and one-bit sparse imaging can be achieved using the SLR-IHT method. The proposed method can also be extended to address one-bit sparse imaging problems of various signal types and imaging scenarios by adapting the construction of the observation matrix $\mathbf{\Phi}$.

Remark 3: Memory requirements. Both the proposed method and existing one-bit CS imaging methods, such as BCST [33], A-BIHT [36], and AS-BIHT [37], require storing the observation matrix $\mathbf{\Phi} \in \mathbf{R}^{2MN \times 2PQ}$. Consequently, directly constructing the observation matrix typically necessitates substantial memory storage, which limits the practical application of these methods in large-scale real-time SAR imaging. To overcome this challenge, a nonuniform fast Fourier transform (NUFFT) based imaging method was proposed in [56] and [57] to expedite the imaging process. This method solely requires storing the interpolation coefficients of NUFFT, thereby obviating the need for direct construction of the observation matrix and effectively reducing memory consumption. Another strategy involves adopting an approximate observation approach by introducing operators based on the MF theory and their corresponding inverse operators to substitute for the computationally intensive matrix–vector multiplications $\mathbf{\Phi}(\cdot)$ and $\mathbf{\Phi}^T(\cdot)$ in (22) [55], [58], [59], [60], [61], [62]. This technique leverages the inherent advantages of both CS methods and MF methods in imaging and achieves memory requirements comparable to traditional MF-based methods. The proposed method can integrate these advancements to further expedite imaging and mitigate memory constraints.

C. Convergence Analysis

To analyze the convergence of the proposed method, we initially present the following Definition and Lemma.

Definition 1 [42]: Let $f(\mathbf{x})$ be a continuously differentiable function. For any vector $\mathbf{x}$ and $\Delta\mathbf{x} \in \mathbb{R}^{2PQ\times 1}$, if the following inequality holds:

$$f(\mathbf{x} + \Delta\mathbf{x}) \le f(\mathbf{x}) + \langle \nabla f(\mathbf{x}), \Delta\mathbf{x}\rangle + \frac{\lambda^*}{2} \| \Delta\mathbf{x} \|_2^2 \tag{30}$$

where $\langle \mathbf{x}, \mathbf{y}\rangle$ represents the inner product of vectors $\mathbf{x}$ and $\mathbf{y}$, then $f(\mathbf{x})$ is said to be strongly smooth with a parameter $\lambda^* > 0$ on the $\mathbb{R}^{2PQ\times 1}$.

Lemma 2 [42]: The sparse logistic loss function is continuously differentiable and strongly smooth on $\mathbb{R}^{2PQ\times 1}$. That is, for any $\mathbf{\Theta}, \mathbf{\Theta}^* \in \mathbb{R}^{2PQ\times 1}$, the following inequality holds:

$$f(\mathbf{\Theta}) \le f\left(\mathbf{\Theta}^*\right) + \langle \nabla f\left(\mathbf{\Theta}^*\right), \mathbf{\Theta} - \mathbf{\Theta}^*\rangle + \frac{\lambda^*}{2} \| \mathbf{\Theta} - \mathbf{\Theta}^* \|_2^2. \tag{31}$$

For the Armijo line search step in Algorithm 1, we have the following Theorem.

Theorem 3: The function $f(\mathbf{\Theta})$ is strongly smooth, given $\mathbf{\Theta}^k \in \mathcal{S}$, where $\mathcal{S}$ is the sparse set defined as $\mathcal{S} = \{\mathbf{\Theta} \in \mathbb{R}^{2PQ\times 1} : \| \mathbf{\Theta} \|_0 \le 2K\}$. Then, for the Armijo line search step in Algorithm 1, the following inequality holds:

$$f\left(\mathbf{\Theta}^k_{\alpha_l}\right) \le f\left(\mathbf{\Theta}^k\right) - \frac{\sigma}{2} \| \mathbf{\Theta}^k_{\alpha_l} - \mathbf{\Theta}^k \|_2^2 \quad \text{for } 0 < \alpha \le \frac{1}{\lambda^* + \sigma}. \tag{32}$$

Therefore, α_l is clearly defined in Algorithm 1.

Proof: According to the computation of $\mathbf{\Theta}^k_{\alpha_l}$ in Algorithm 1, we have

$$\mathbf{\Theta}^k_{\alpha_l} \in \operatorname{argmin}\left\{ \left\| \mathbf{\Theta} - \mathbf{\Theta}^k + \alpha \nabla f\left(\mathbf{\Theta}^k\right) \right\|_2^2 : \mathbf{\Theta} \in \mathcal{S} \right\} \tag{33}$$

which implies that $\| \mathbf{\Theta}^k_{\alpha_l} - \mathbf{\Theta}^k + \alpha \nabla f(\mathbf{\Theta}^k) \|_2^2 \le \| \alpha \nabla f(\mathbf{\Theta}^k) \|_2^2$ through $\mathbf{\Theta}^k \in \mathcal{S}$. This leads to

$$\left\| \mathbf{\Theta}^k_{\alpha} - \mathbf{\Theta}^k \right\|_2^2 \le -2\alpha \left\langle \nabla f\left(\mathbf{\Theta}^k\right), \mathbf{\Theta}^k_{\alpha} - \mathbf{\Theta}^k \right\rangle. \tag{34}$$

From the strong smoothness property of $f(\mathbf{\Theta})$ and (34), we can derive that

$$\begin{aligned} f\left(\mathbf{\Theta}^k_{\alpha_l}\right) &\le f\left(\mathbf{\Theta}^k\right) + \left\langle \nabla f\left(\mathbf{\Theta}^k\right), \mathbf{\Theta}^k_{\alpha_l} - \mathbf{\Theta}^k \right\rangle \\ &\quad + \frac{\lambda^*}{2} \left\| \left(\mathbf{\Theta}^k_{\alpha_l} - \mathbf{\Theta}^k\right) \right\|_2^2 \\ &\le f\left(\mathbf{\Theta}^k\right) - \frac{1}{2\alpha} \| \mathbf{\Theta}^k_{\alpha_l} - \mathbf{\Theta}^k \|_2^2 + \frac{\lambda^*}{2} \left\| \left(\mathbf{\Theta}^k_{\alpha_l} - \mathbf{\Theta}^k\right) \right\|_2^2 \\ &= f\left(\mathbf{\Theta}^k\right) - \frac{1}{2}\left(1/\alpha - \lambda^*\right) \| \mathbf{\Theta}^k_{\alpha_l} - \mathbf{\Theta}^k \|_2^2. \end{aligned} \tag{35}$$

By constraining $\alpha \in (0, (1/\lambda^* + \sigma)]$, we obtain the desired result. □

In the kth iteration, when utilizing Algorithm 1 to estimate $\mathbf{\Theta}^k_{\alpha_l}$, we subsequently apply the greedy selection rule $\mathbf{\Theta}^{k+1} = \Gamma(\mathbf{\Theta}^k_{\alpha_l}, K)$ to ensure joint sparsity constraints. Let

$\boldsymbol{\Theta}^{k+1} + \Delta\boldsymbol{\Theta}^k = \boldsymbol{\Theta}^k_{\alpha_l}$, where $\Delta\boldsymbol{\Theta}^k$ contains only a few nonzero elements, and the position indices of these elements are denoted as $T_{\Delta\boldsymbol{\Theta}^k}$. According to Lemma 2, there exists λ^* such that

$$f\left(\boldsymbol{\Theta}^{k+1}\right) \le f\left(\boldsymbol{\Theta}^k_{\alpha_l}\right) + \left\langle \nabla f\left(\boldsymbol{\Theta}^k_{\alpha_l}\right), \Delta\boldsymbol{\Theta}^k \right\rangle + \frac{\lambda^*}{2}\left\|\Delta\boldsymbol{\Theta}^k\right\|_2^2. \tag{36}$$

Given that $f(\boldsymbol{\Theta}^k_{\alpha_l})$ satisfies (32) and $\langle \nabla f(\boldsymbol{\Theta}^k_{\alpha_l}), \Delta\boldsymbol{\Theta}^k \rangle = \sum_{i\in T_{\Delta\boldsymbol{\Theta}^k}} \nabla_i f(\boldsymbol{\Theta}^k_{\alpha_l}) \Delta\Theta^k_i$ tends to zero [44], [63], substituting (32) into (36) yields

$$f\left(\boldsymbol{\Theta}^{k+1}\right) \le f\left(\boldsymbol{\Theta}^k\right) - \frac{\sigma}{2}\left\|\boldsymbol{\Theta}^k_{\alpha_l} - \boldsymbol{\Theta}^k\right\|^2 + \frac{\lambda^*}{2}\left\|\Delta\boldsymbol{\Theta}^k\right\|_2^2. \tag{37}$$

When $\sigma \| \boldsymbol{\Theta}^k_{\alpha_l} - \boldsymbol{\Theta}^k \|_2^2 - \lambda^* \| \Delta\boldsymbol{\Theta}^k \|_2^2 \ge 0$, we have $f(\boldsymbol{\Theta}^{k+1}) \le f(\boldsymbol{\Theta}^k)$, indicating that the $f(\boldsymbol{\Theta})$ consistently decreases with an increasing number of iterations. In Section IV, we conducted cross-validation and experimental analysis of algorithm parameters σ and β. Furthermore, we performed experimental verification of the convergence of the proposed method under these reference parameter settings using various simulated and real radar data.

D. Computational Complexity Analysis

Let $I = PQ$ represent the total number of imaging pixels and $J = MN$ for the total number of transmitted frequencies, so that $\boldsymbol{\Phi} \in \mathbb{R}^{2J\times 2I}$, $\mathbf{z} \in \mathbb{R}^{2J\times 1}$, and $\boldsymbol{\Theta} \in \mathbb{R}^{2I\times 1}$ hold. For the proposed SLR-IHT method, the computational complexity of the joint sparse constraint step $\Gamma(\boldsymbol{\Theta}, K)$ is negligible relative to the Armijo line search and gradient calculation. Since the operation is constrained to the support set T_K, the computational complexity of the Armijo line search is about $\mathcal{O}(4JKl)$, where l is the number of iterations, which is typically set to no more than 15. The main cost of calculating gradient is to compute $\boldsymbol{\Phi}^T\mathbf{z}$, approximately $\mathcal{O}(4IJ)$. Thus, each iteration of SLR-IHT has a total computational cost of approximately $\mathcal{O}(4J(Kl + I))$.

The computational complexity of the SLR-IHT method is compared with the three state-of-the-art one-bit CS imaging methods, BCST [33], A-BIHT [36], and AS-BIHT [37]. Both A-BIHT and AS-BIHT methods are based on the BIHT method framework. According to (12), each iteration of the BIHT method involves the $\boldsymbol{\Phi}(\cdot)$ and $\boldsymbol{\Phi}^T(\cdot)$ operation, and the main computational complexity is $\mathcal{O}(8JI)$. The proposed method usually satisfies the $Kl \ll I$, so the computational complexity is lower than that of the BIHT method. In each iteration, the A-BIHT method additionally needs to build support sets for consistency and inconsistencies, and the AS-BIHT method needs to generate additional adversarial samples and adjust the quantization level, both of which require $\boldsymbol{\Phi}(\cdot)$ and $\boldsymbol{\Phi}^T(\cdot)$ operations. Therefore, the computational complexity of these two methods is higher than that of the BIHT method. The BCST method needs to calculate the matrix inversion $(\boldsymbol{\Phi}\boldsymbol{\Phi}^T + \mu\mathbf{I}_{2M})^{-1}$ before iteration, where μ is the regularization parameter, and the computational complexity is about $\mathcal{O}(8/3J^3)$. In the iterative process, the computational complexity of the BCST method is approximately $\mathcal{O}(8IJ + 8J^2)$. By comparison, it is proved that the proposed method has a lower computational complexity per iteration than current methods.

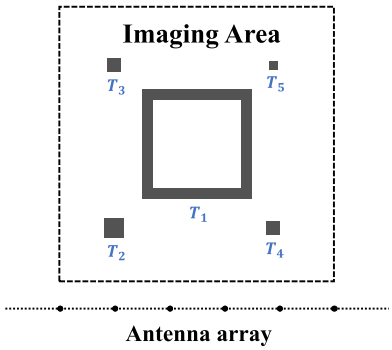

Fig. 1. Imaging scene of a simulation experiment.

IV. Numerical Results

In order to verify the effectiveness of the proposed method in one-bit SAR imaging, this section presents experimental results using both simulated and real radar data. We compare the performance of the proposed SLR-IHT method with that of the traditional back-projection (BP) method, as well as the one-bit CS-based imaging methods, BCST [33], A-BIHT [36], and AS-BIHT [37]. The reconstructed images obtained from each method are normalized for fair comparison. All experiments are conducted on a personal computer equipped with an Intel Core[1] i9-13900HX processor and 64 GB of RAM.

A. Simulation Data Experiment

We first generated a simulated imaging scene to evaluate the performance of all methods. To quantitatively compare the imaging performance of the proposed method and the comparison methods, we employed mean square error (MSE) and target-to-clutter ratio (TCR). MSE is defined as follows [37]:

$$\text{MSE} = 10\log_{10}\left(\left\|\boldsymbol{\Theta} - \widehat{\boldsymbol{\Theta}}\right\|_2/(PQ)\right) \tag{38}$$

where $\boldsymbol{\Theta}$ represents the normalized ground truth and $\widehat{\boldsymbol{\Theta}}$ represents the reconstructed results. A lower MSE indicates a smaller reconstruction error and higher imaging quality. TCR is defined as [37]

$$\text{TCR} = 10\log_{10}\frac{(1/P_T)\sum_{(x,y)\in T}|\boldsymbol{\Theta}_T|^2}{(1/P_C)\sum_{(x,y)\in C}|\boldsymbol{\Theta}_C|^2} \tag{39}$$

where $\boldsymbol{\Theta}_T$ and $\boldsymbol{\Theta}_C$ represent the amplitudes of pixels in the target and clutter regions, respectively, while P_T and P_C are the respective number of pixels. A higher TCR value indicates a stronger concentration of dominant coefficients in the target region, resulting in a reduction of artifacts outside this region. To compute TCR, we select the target and clutter regions based on the known ground-truth positions of the targets.

Since one-bit CS-based imaging methods require only a small number of measurements to achieve highly accurate

[1]Trademarked.

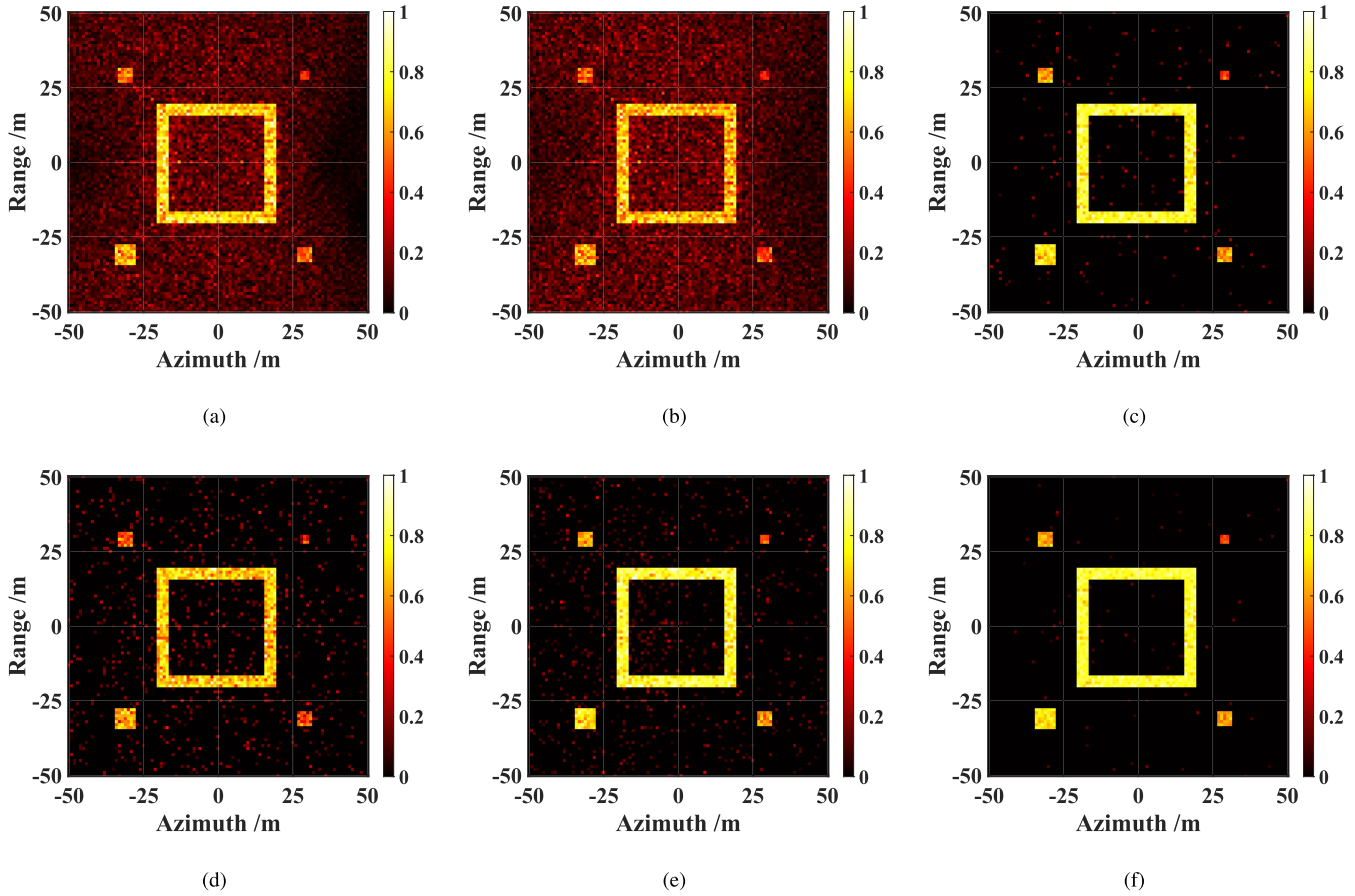

Fig. 2. One-bit SAR imaging result of the simulated scene ($K = 800$, SNR $= 20$ dB, SR $= 25\%$). (a) BP, (b) BP (one bit), (c) BCST, (d) A-BIHT, (e) AS-BIHT, and (f) SLR-IHT.

imaging of sparse scenes, we introduce the sampling ratio (SR) to measure the proportion of randomly sampled data [64]

$$\mathrm{SR} = \frac{\text{Randomly selected amount of data}}{\text{Total amount of data}} \times 100\%. \quad (40)$$

The SNR of simulation experiment data adopts the definition in [65], [66], and [67]

$$\mathrm{SNR} = 10\log_{10}\frac{\mathrm{E}\|\boldsymbol{\Phi}\boldsymbol{\Theta}\|_2^2}{\mathrm{E}\|\mathbf{w}\|_2^2}. \quad (41)$$

1) Simulation Experiments: The imaging area in the simulation was chosen to be 100×100 m, divided into a grid of $P \times Q = 101 \times 101$ pixels with a grid spacing of 1 m per pixel. There were a total of 20 antenna positions and 2001 frequency points, with an aperture length of 200 m. The frequency sweep was conducted with a 1-MHz step size, covering the frequency range from 5 to 7 GHz, resulting in a bandwidth of 2 GHz. The imaging scene consisted of five targets, occupying a total of 684 pixels, as illustrated in Fig. 1. All target scattering coefficients were normalized. Target T_1 occupied 576 positions with a scattering coefficient of 1. Target T_2 comprised a grid of size 7×7 with a scattering coefficient of 0.8. Targets T_3 and T_4 consisted of grids of size 5×5 with a scattering coefficient of 0.6. Compared to the other targets, T_5 was a small target occupying a 3×3 grid with a scattering coefficient of 0.4. The termination conditions for BCST, A-BIHT, and AS-BIHT were set as a maximum of 200 iterations or when the kth iteration satisfied $(|\boldsymbol{\Theta}^k - \boldsymbol{\Theta}^{k-1}|_2/|\boldsymbol{\Theta}^k|_2) < 10^{-6}$.

TABLE I
QUANTITATIVE COMPARISON OF IMAGING RESULTS OF DIFFERENT METHODS IN SIMULATION SCENE

	BP	BP (one bit)	BCST	ABIHT	ASBIHT	SLR-IHT
MSE (dB)	-28.5563	-28.0848	-32.3324	-30.3063	-31.9254	**-32.9287**
TCR (dB)	15.0709	13.6855	31.1421	23.0355	26.5657	**35.7531**

We set the SR $= 25\%$ and the SNR $= 20$ dB in the simulation experiments. For the proposed method, A-BIHT and AS-BIHT, we fixed the sparsity level $K = 800$. Fig. 2(a) and (b) illustrates the imaging results obtained using the complete quantized data and the one-bit quantized data with the BP method, respectively, revealing the presence of high sidelobe levels. In contrast, the one-bit CS-based methods, including BCST, A-BIHT, AS-BIHT, and our proposed method, successfully estimated all the scattering points. However, BCST, A-BIHT, and AS-BIHT methods exhibited varying degrees of artifacts. In contrast, the proposed SLR-IHT method demonstrated cleaner backgrounds and a better representation of the differences in scattering intensity among the five targets. Table I presents the MSE and TCR values for all the images in Fig. 2, further confirming the quantitative evaluation results that the proposed method achieved the lowest MSE and the highest TCR. This is because the

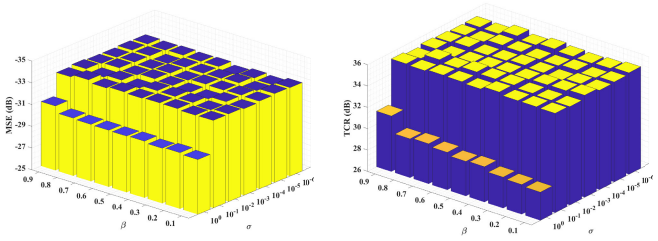

(a) (b)

Fig. 3. Quantitative evaluation of MSE and TCR values for the imaging results of the proposed method with different parameter configurations. (a) MSE. (b) TCR.

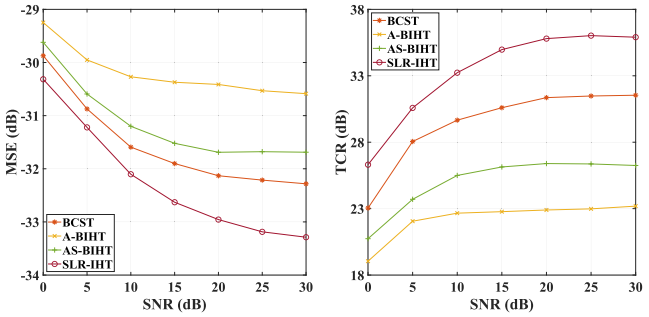

(a) (b)

Fig. 4. MSE and TCR variation curves with SNR, where the SR $= 25\%$ and $K = 800$. (a) MSE. (b) TCR.

proposed method is based on the SLR model, which utilizes a differentiable nonlinear logistic function to learn and represent the nonlinear patterns. It provides an excellent alternative to the sign(·) function and improves imaging results. Moreover, our method incorporates joint sparsity constraints on the real and imaginary parts, effectively suppressing the occurrence of artifacts.

2) Imaging Performance With Different Parameter Configurations: The parameters involved in the Armijo line search step of Algorithm 1 for the proposed method include σ and β. σ primarily controls the level of reduction in the objective function $f(\boldsymbol{\Theta})$, while β governs the rate of change in the step size. To evaluate the influence of the parameters σ and β on the performance of the SLR-IHT method, we conducted experimental analysis using the simulated data corresponding to Fig. 2. The parameter σ was varied within the range of $[10^0, 10^{-1}, 10^{-2}, 10^{-3}, 10^{-4}, 10^{-5}, 10^{-6}]$, while β was varied within the range of $[0.1, 0.2, 0.3, 0.4, 0.5, 0.6, 0.7, 0.8, 0.9]$. Fig. 3 illustrates the quantitative evaluation results with different σ and β values, based on 50 Monte Carlo random trials and the calculated mean values. The observations show that when σ is fixed at 10^0, the imaging results consistently exhibit poor quantitative evaluation, characterized by higher MSE and lower TCR, regardless of the chosen β value. However, for σ values less than or equal to 10^{-1}, the SLR-IHT method achieves superior imaging performance and demonstrates robustness in the selection of β. Based on these findings, we selected $\sigma = 10^{-4}$ and $\beta = 0.8$ as the parameter settings for subsequent imaging experiments in our proposed method.

In the subsequent simulations, we conduct Monte Carlo random trials to study the imaging performance of different

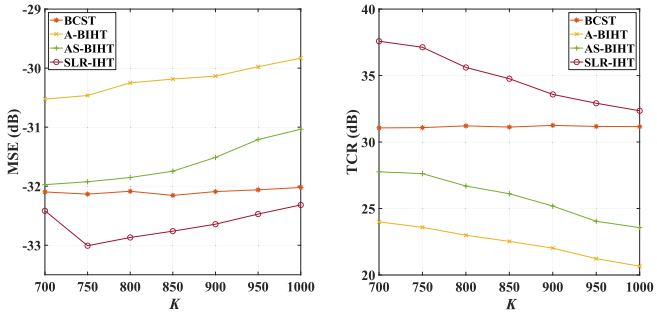

(a) (b)

Fig. 5. MSE and TCR variation curves with the sparsity levels K, where the SR $= 25\%$ and SNR $= 20$ dB. (a) MSE. (b) TCR.

methods with various conditions, including different SNR, SR, and sparsity level K. The experiments are repeated 50 times, with the measurement data being regenerated for each trial, and the results of all methods are averaged for analysis.

3) Imaging Performance With Different SNRs: Fig. 4 presents all one-bit CS-based methods' imaging performance curves as the SNR varies, with SR $= 25\%$ and $K = 800$. It is evident that the imaging performance of all methods improves with increasing SNR. Notably, the proposed SLR-IHT method exhibits significant advantages in terms of MSE and TCR compared to the other comparative methods. While the BCST method outperforms AS-BIHT and A-BIHT in terms of imaging performance, it requires storing time-variable thresholding, which introduces an additional system burden. On the other hand, AS-BIHT adaptively adjusts the quantization level parameter by consistently reconstructing the updated imaging scene and corresponding adversarial samples in each iteration, resulting in improved imaging quality compared to A-BIHT.

4) Imaging Performance With Different Sparsity Levels K: The proposed methods, AS-BIHT and A-BIHT, are all greedy selection methods that require setting the sparsity level K as an input parameter. Given that the actual count of scattering points within the scene is 684, it is imperative to select a sparsity level parameter K greater than 684 to ensure complete imaging. In Fig. 5, we analyze the relationship between imaging performance and the sparsity level K for all methods, with SR $= 25\%$ and SNR $= 20$ dB. When K was set to 700, slightly exceeding the actual count of scatter points, the proposed method exhibited limitations in effectively estimating certain weak scatter points within the scene. This led to a relatively higher MSE, although it remained lower than that of the comparative methods. Notably, this was due to the concentration of estimated scatter points within the target region $\boldsymbol{\Theta}_T$, thus maintaining a relatively high TCR. When $K = 750$, the proposed method exhibited enhanced capabilities in effectively estimating all scatter points within the scene while adeptly suppressing clutter, resulting in the lowest MSE. As sparsity level K continues to increase, the SLR-IHT, A-BIHT, and AS-BIHT methods retain a higher number of scatter points than the actual count within the scene, leading to increased MSE and decreased TCR. Consequently, when choosing the sparsity level K for the scene, opting for a value slightly greater than the actual count of scatter points

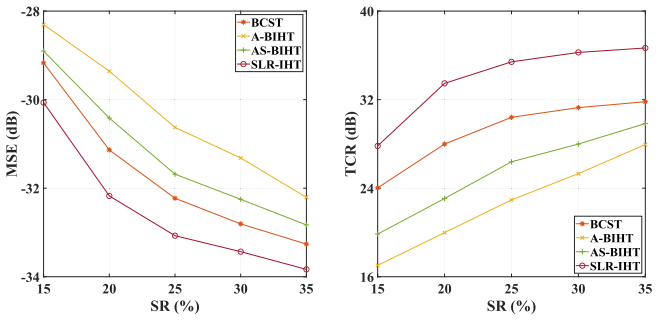

(a) (b)

Fig. 6. MSE and TCR variation curves with SR, where the SNR = 20 dB and $K = 800$. (a) MSE. (b) TCR.

proves effective in achieving improved imaging performance with these greedy selection methods. The BCST algorithm, independent of the sparsity level K, maintains stable MSE and TCR values regardless of changes in the sparsity level K.

5) Imaging Performance With Different SRs: Fig. 6 presents the investigation of imaging quality with different SRs, with SNR = 20 dB and $K = 800$. It is evident that the imaging performance of all methods improves as the SR increases. Both evaluation metrics consistently demonstrate the same conclusion regarding imaging performance assessment. Similar to the findings in Figs. 4 and 5, the proposed method exhibits superior imaging performance compared to the comparison methods across both evaluation metrics. With the increase in SR, the AS-BIHT method achieves better adjustment of the quantization level parameter, resulting in improved imaging performance that surpasses that of the A-BIHT method.

B. Real Data Experiments

This section presents a comparative analysis of the imaging results obtained from two sets of real radar data. Due to the unavailability of the true scattering values in the real data and the challenge of accurately delineating the target region, we evaluate the imaging quality using the following metrics [64], [68]:

$$\text{Entropy} = -\sum_{p=1}^{P}\sum_{q=1}^{Q}\frac{\left|\widehat{\Theta}_{pq}\right|^2}{\left\|\widehat{\boldsymbol{\Theta}}\right\|_2^2}\log\frac{\left|\widehat{\Theta}_{pq}\right|^2}{\left\|\widehat{\boldsymbol{\Theta}}\right\|_2^2}. \tag{42}$$

A smaller value of entropy indicates better focusing quality. In addition, the maximum iteration count for all methods was capped at 50.

1) First Set of Real Data Imaging Experiments: The first set of experiments was conducted in a microwave anechoic chamber. A pair of Archimedes helical antennas are used to transmit and receive radar signals at a distance of 0.79 m and a height of 1.33 m relative to the target plane. A stepped frequency signal with a step size of 1 MHz was utilized, covering the frequency range of 0.5–2.5 GHz. Fig. 7(a) depicts the target distribution in the imaging region, and Fig. 7(b) depicts the geometry of the imaging scene. There are five distinct objects in the scene, including two dihedral reflectors (T_1, T_2), two trihedral reflectors (T_1, T_2), and a metal sphere T_5. Notably, T_5 was considerably smaller than the other targets.

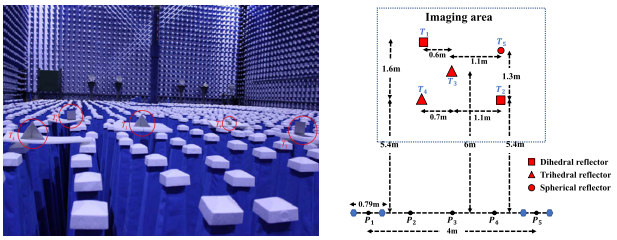

(a) (b)

Fig. 7. (a) Target distribution. (b) Geometry of the imaging scene.

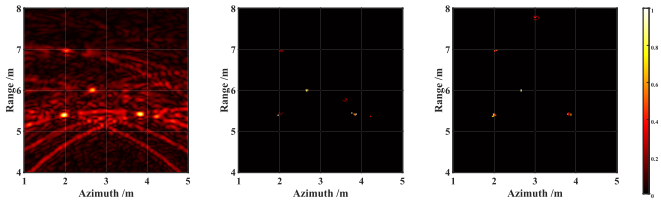

(a) (b) (c)

Fig. 8. Imaging results of the first set of real data. (a) BP, uses fully one-bit quantized data. (b) BCST, SR = 25%. (c) BCST, SR = 50%.

TABLE II
ENTROPY COMPARISON OF IMAGING RESULTS FROM DIFFERENT METHODS (FIRST SET OF REAL DATA)

SR	K	BCST	A-BIHT	AS-BIHT	SLR-IHT
25%	20	0.0263	0.0262	0.0261	**0.0140**
	25		0.0317	0.0319	0.0175
	30		0.0379	0.0373	0.0211
50%	20	0.0255	0.0267	0.0261	**0.0141**
	25		0.0324	0.0317	0.0175
	30		0.0382	0.0376	0.0209

The imaging area measures 4 × 4 m, while the number of image grids is 150 × 150.

In Fig. 8, we compare the imaging results of the BP method and the BCST method with different SRs. Fig. 9 presents the imaging results obtained using the A-BIHT, AS-BIHT, and our proposed method with various SRs and sparsity level K. From Figs. 8 and 9, it can be observed that the BP method suffers from significant blurring and artifacts, and both the BCST and A-BIHT methods fail to effectively estimate the target T_5. As the SR increases from 25% to 50%, the AS-BIHT method effectively estimates all targets, but there is still a certain degree of blurring artifacts, as shown in Fig. 9(e). In contrast, our proposed method consistently and effectively estimates all targets with lower sparsity level K and SR conditions. To quantify the imaging results, we calculate each method's entropy values, as listed in Table II. It can be observed that with the same SR, increasing the sparsity level K leads to higher entropy values for A-BIHT, AS-BIHT, and the proposed method. However, our method consistently maintains smaller entropy values, indicating superior focusing quality and effective artifact suppression.

Furthermore, we note that increasing the SR from 25% to 50% does not significantly impact the entropy values for all methods with the same sparsity level K. This demonstrates that 25% of the data is sufficient to achieve satisfactory

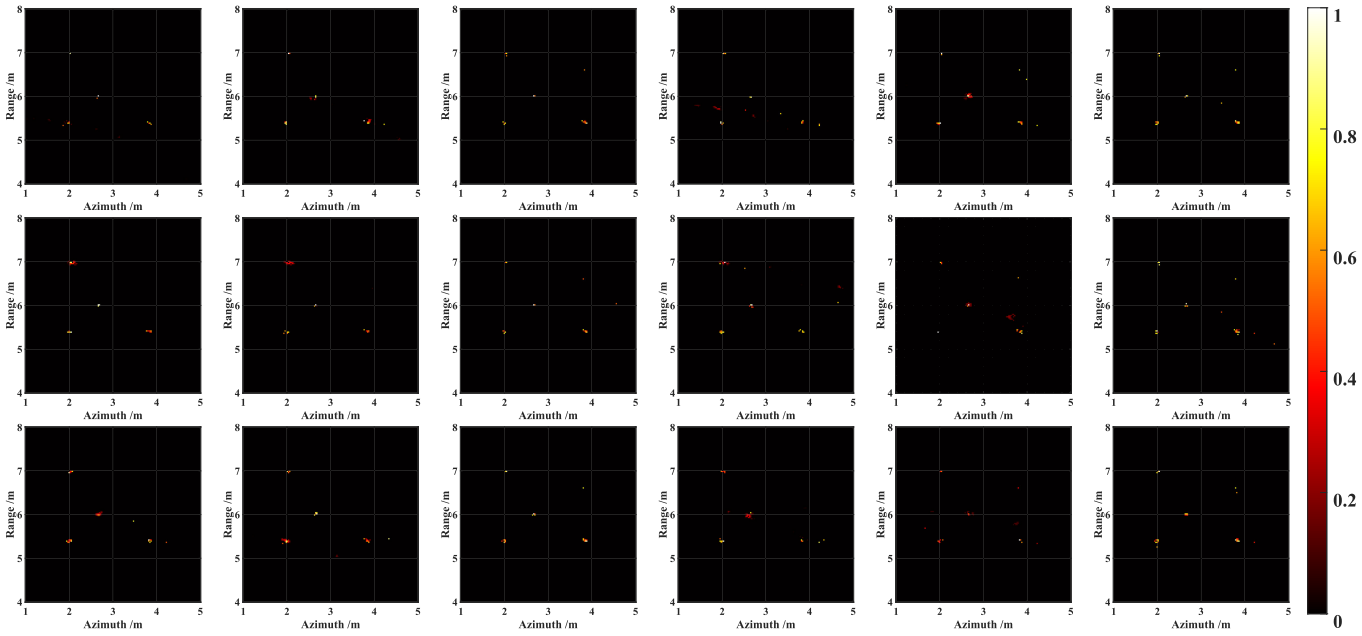

Fig. 9. Imaging results of the first set of real data. From top to bottom, the sparsity levels are $K = 20$, 25, and 30. (a) A-BIHT, SR = 25%, (b) AS-BIHT, SR = 25%, (c) SLR-IHT, SR = 25%, (d) A-BIHT, SR = 50%, (e) AS-BIHT, SR = 50%, and (f) SLR-IHT, SR = 50%.

TABLE III
COMPARISON OF TIME CONSUMPTION OF DIFFERENT METHODS (FIRST SET OF REAL DATA)

SR	K	BCST (s)	A-BIHT (s)	AS-BIHT (s)	SLR-IHT (s)
25%	20	10.3265	25.5998	72.5073	**1.7524**
	25				1.8186
	30				1.8383
50%	20	39.4386	56.6727	172.3457	**3.3212**
	25				3.3702
	30				3.3748

imaging results and highlights the advantage of CS methods, which enable effective imaging with limited measurements. In addition, we conducted a comparison of the time consumption among different methods with various SRs, as shown in Table III. The results demonstrate that our proposed SLR-IHT method is significantly less time-consuming than other methods. This advantage is attributed to the fact that the proposed method performs iterative optimization on a smaller support set, and the computational complexity depends on the size of the support set, i.e., the sparsity level K. When K is small, the time consumption is consequently reduced.

2) Second Set of Real Data Imaging Experiments: In order to further validate the imaging effectiveness of various methods in dealing with complex targets, the second set of imaging experiments uses a set of wrench data for one-bit SAR imaging. The optical image of the wrench model employed in the experiment is depicted in Fig. 10. For data acquisition, a linear frequency-modulated continuous wave (FMCW) signal spanning the frequency range of 77–81 GHz was employed, with 256 samples. The imaging region was defined as 0.45 × 0.45 m, with a scene size of 150 × 150 and a pixel spacing of 0.003 m. The primary scattering bodies in the scene comprised the wrench itself and its fixed base. For the normalized imaging results, we take the logarithm to display.

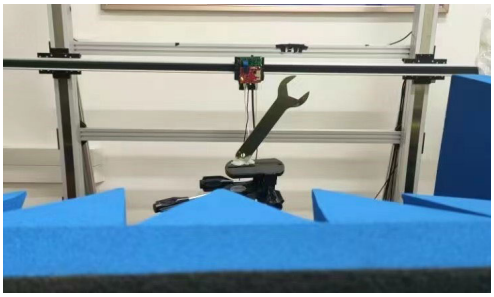

Fig. 10. Optical image of the wrench model.

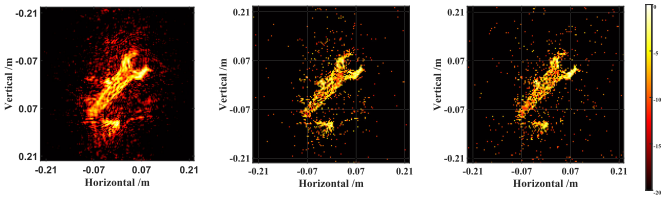

Fig. 11. Imaging results of the second set of real data. (a) BP, uses fully one-bit quantized data, (b) BCST, SR = 25%, and (c) BCST, SR = 50%.

Similar to the first set of real data experiments, we present the imaging results using the BP and BCST methods in Fig. 11. Additionally, Fig. 12 showcases the imaging results obtained using the proposed, A-BIHT, and AS-BIHT methods with different sparsity levels K and SR. The results demonstrate that, compared to the conventional BP method, the CS-based methods require only a small number of measurements to effectively estimate the contours of the targets.

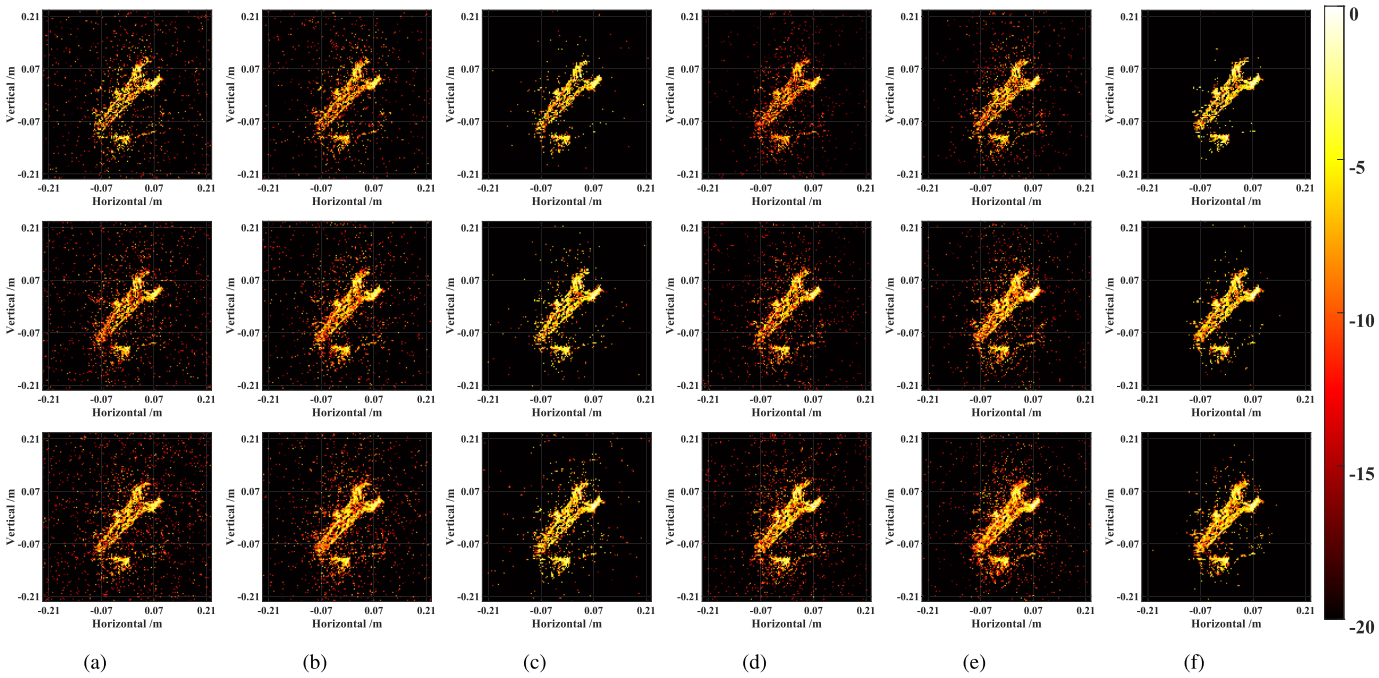

Fig. 12. Imaging results of the second set of real data. From top to bottom, the sparsity levels are $K = 1000$, 1250, and 1500. (a) A-BIHT, SR = 25%, (b) AS-BIHT, SR = 25%, (c) SLR-IHT, SR = 25%, (d) A-BIHT, SR = 50%, (e) AS-BIHT, SR = 50%, and (f) SLR-IHT, SR = 50%.

TABLE IV
ENTROPY COMPARISON OF IMAGING RESULTS FROM DIFFERENT METHODS (SECOND SET OF REAL DATA)

SR	K	BCST	A-BIHT	AS-BIHT	SLR-IHT
25%	1000	0.7582	1.0087	0.9902	**0.5844**
	1250		1.2093	1.1841	0.7141
	1500		1.4144	1.3732	0.8401
50%	1000	0.7449	0.9843	0.9784	**0.5823**
	1250		1.1896	1.1651	0.7123
	1500		1.3833	1.3361	0.8356

TABLE V
COMPARISON OF TIME CONSUMPTION OF DIFFERENT METHODS (SECOND SET OF REAL DATA)

SR	K	BCST (s)	A-BIHT (s)	AS-BIHT (s)	SLR-IHT (s)
25%	1000	478.0423	119.6747	747.4434	**19.7392**
	1250				24.4886
	1500				26.8254
50%	1000	980.2744	232.5721	1338.5143	**25.8689**
	1250				29.7776
	1500				31.5501

Among the CS-based methods, the proposed method exhibits clearer imaging results of the wrench and its base, effectively suppressing clutter and artifacts, and concentrating the dominant coefficients at the positions of real scatterers. In contrast, the imaging results of the compared AS-BIHT method, A-BIHT method, and BCST method still exhibit more artifacts. Regarding the proposed method, the A-BIHT method, and the AS-BIHT method based on greedy selection rules, as the sparsity level K increases, the contours of the targets in the imaging results become clearer. However, due to the increased number of retained scatter points, the occurrence of clutter and artifacts becomes more severe. Notably, the proposed method performs better in suppressing clutter and artifacts than the compared methods. The imaging results with different sparsity levels K indicate that the proposed method achieves good imaging results across a wide range of sparsity levels.

The entropy values for all imaging results obtained using different methods are documented in Table IV. The results indicate a slight decrease in entropy for all CS-based imaging methods with an increase in SR, implying an improvement in imaging quality with a larger amount of available data. Moreover, Fig. 12 demonstrates that the contours of the imaging results become sharper as the SR increases. Notably, the proposed method consistently exhibits the lowest entropy value compared to the A-BIHT and AS-BIHT methods, showcasing its effectiveness in accurately focusing on targets and suppressing artifacts. In Table V, we present a comparison of the time consumption among all CS-based methods, highlighting the significant advantage of the proposed method in terms of imaging efficiency. Moreover, the computational complexity of the proposed method is closely tied to the sparsity level K, resulting in increased computation time as K significantly increases. Although the entropy of the proposed method at $K = 1500$ appears higher than that of the BCST method in Table IV, a closer examination in Table V reveals that the time consumption of BCST is substantially higher than that of the proposed method.

C. Convergence Performance Analysis

In this section, we validate the convergence of the proposed method through simulations and experimental data

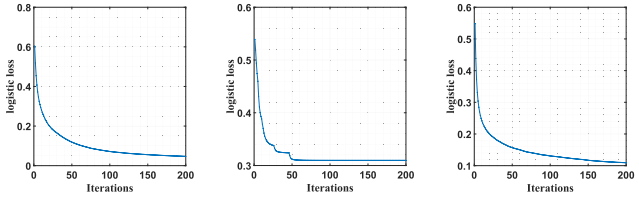

(a) (b) (c)

Fig. 13. Logistic loss curve of the proposed method with the number of iterations. (a) Simulated data with SNR = 20 dB, $K = 800$, SR = 25%. (b) First set of real data with $K = 20$, SR = 25%. (c) Second set of real data with $K = 1250$, SR = 25%.

experiments. The logistic loss is defined as

$$\text{Logistic loss} = \frac{1}{2MN}\sum_{i=1}^{2MN}\log\left(1+\exp\left(-z_i\cdot\left(\mathbf{\Phi}_{i,:}\mathbf{\Theta}\right)\right)\right). \tag{43}$$

Fig. 13 illustrates the logistic loss curve of the proposed method for 200 iterations when imaging simulated data and two sets of real data. It can be observed that the logistic loss of the proposed method continuously decreases with an increasing number of iterations. Even when dealing with imaging data of different scales, the proposed method typically significantly reduces logistic loss after less than 20 iterations and gradually stabilizes after fewer than 50 iterations. This indicates that the proposed method exhibits good convergence performance in handling imaging tasks.

V. Conclusion

In this article, we present the application of the SLR model in the field of one-bit SAR imaging, combined with the classical IHT method, to achieve high-quality imaging results. To accelerate the computational process, we utilize the Armijo line search during the iterative optimization process. Additionally, the introduction of joint sparsity constraints on the real and imaginary parts effectively suppresses artifacts in the reconstructed images. The convergence of the proposed method is also analyzed theoretically. Extensive simulations and imaging experiments using real radar data demonstrate that our proposed method outperforms existing state-of-the-art one-bit SAR imaging methods in terms of imaging quality and time consumption. This emphasizes the feasibility and superiority of our approach in addressing the challenges of one-bit SAR imaging. Furthermore, the proposed method employs zero thresholding for one-bit quantization, reducing the complexity of the imaging system compared to methods using time-varying thresholds.

Acknowledgment

The authors sincerely thank the associate editor and the referees for their constructive comments, which have significantly improved the quality of the article.

References

[1] H. E. Güven, A. Güngör, and M. Çetin, "An augmented Lagrangian method for complex-valued compressed SAR imaging," *IEEE Trans. Comput. Imag.*, vol. 2, no. 3, pp. 235–250, Sep. 2016.

[2] N. Jiang, D. Feng, J. Wang, J. Zhu, and X. Huang, "Along-track swarm SAR: Echo modeling and sub-aperture collaboration imaging based on sparse constraints," *IEEE J. Sel. Topics Appl. Earth Observ. Remote Sens.*, vol. 16, pp. 5602–5617, 2023.

[3] G. Xu, L. Yang, G. Bi, and M. Xing, "Enhanced ISAR imaging and motion estimation with parametric and dynamic sparse Bayesian learning," *IEEE Trans. Comput. Imag.*, vol. 3, no. 4, pp. 940–952, Dec. 2017.

[4] N. Jiang, J. Wang, D. Feng, N. Kang, and X. Huang, "SAR imaging method for moving target with azimuth missing data," *IEEE J. Sel. Topics Appl. Earth Observ. Remote Sens.*, vol. 15, pp. 7100–7113, 2022.

[5] L. Kang, B.-S. Liang, Y. Luo, and Q. Zhang, "Sparse imaging for spinning space targets with short time observation," *IEEE Sensors J.*, vol. 21, no. 7, pp. 9090–9098, Apr. 2021.

[6] Y. Zhang and M. Xing, "Joint method of ISAR imaging and scaling for maneuvering targets via compressive sensing," *IEEE Sensors J.*, vol. 19, no. 17, pp. 7300–7307, Sep. 2019.

[7] J. Rong, Y. Wang, and T. Han, "Iterative optimization-based ISAR imaging with sparse aperture and its application in interferometric ISAR imaging," *IEEE Sensors J.*, vol. 19, no. 19, pp. 8681–8693, Oct. 2019.

[8] H. Du et al., "A novel SAR ground maneuvering target imaging method based on adaptive phase tracking," *IEEE Trans. Geosci. Remote Sens.*, vol. 61, 2023, Art. no. 5211916.

[9] S. J. Zahabi, M. M. Naghsh, M. Modarres-Hashemi, and J. Li, "One-bit compressive radar sensing in the presence of clutter," *IEEE Trans. Aerosp. Electron. Syst.*, vol. 56, no. 1, pp. 167–185, Feb. 2020.

[10] X. Wang, G. Li, Y. Liu, and M. G. Amin, "Enhanced 1-bit radar imaging by exploiting two-level block sparsity," *IEEE Trans. Geosci. Remote Sens.*, vol. 57, no. 2, pp. 1131–1141, Feb. 2019.

[11] B. Zhao, L. Huang, and W. Bao, "One-bit SAR imaging based on single-frequency thresholds," *IEEE Trans. Geosci. Remote Sens.*, vol. 57, no. 9, pp. 7017–7032, Sep. 2019.

[12] A. Ameri, A. Bose, J. Li, and M. Soltanalian, "One-bit radar processing with time-varying sampling thresholds," *IEEE Trans. Signal Process.*, vol. 67, no. 20, pp. 5297–5308, Oct. 2019.

[13] F. Xi, Y. Xiang, S. Chen, and A. Nehorai, "Gridless parameter estimation for one-bit MIMO radar with time-varying thresholds," *IEEE Trans. Signal Process.*, vol. 68, pp. 1048–1063, 2020.

[14] B. Zhao, L. Huang, J. Li, M. Liu, and J. Wang, "Deceptive SAR jamming based on 1-bit sampling and time-varying thresholds," *IEEE J. Sel. Topics Appl. Earth Observ. Remote Sens.*, vol. 11, no. 3, pp. 939–950, Mar. 2018.

[15] B. Zhao, L. Huang, and B. Jin, "Strategy for SAR imaging quality improvement with low-precision sampled data," *IEEE Trans. Geosci. Remote Sens.*, vol. 59, no. 4, pp. 3150–3160, Apr. 2021.

[16] J. Han, G. Li, and X.-P. Zhang, "Refocusing of moving targets based on low-bit quantized SAR data via parametric quantized iterative hard thresholding," *IEEE Trans. Aerosp. Electron. Syst.*, vol. 56, no. 3, pp. 2198–2211, Jun. 2020.

[17] X. Huang and B. Liao, "One-bit MUSIC," *IEEE Signal Process. Lett.*, vol. 26, no. 7, pp. 961–965, Jul. 2019.

[18] S. Ge, C. Fan, J. Wang, and X. Huang, "Low-complexity one-bit DOA estimation for massive ULA with a single snapshot," *Remote Sens.*, vol. 14, no. 14, p. 3436, Jul. 2022.

[19] Z. Wei, W. Wang, F. Dong, and Q. Liu, "Gridless one-bit direction-of-arrival estimation via atomic norm denoising," *IEEE Commun. Lett.*, vol. 24, no. 10, pp. 2177–2181, Oct. 2020.

[20] L. Chu, F. Wen, L. Li, and R. Qiu, "Efficient nonlinear precoding for massive MIMO downlink systems with 1-bit DACs," *IEEE Trans. Wireless Commun.*, vol. 18, no. 9, pp. 4213–4224, Sep. 2019.

[21] J. Li, M. M. Naghsh, S. J. Zahabi, and M. Modarres-Hashemi, "Compressive radar sensing via one-bit sampling with time-varying thresholds," in *Proc. 50th Asilomar Conf. Signals, Syst. Comput.*, 2016, pp. 1164–1168.

[22] G. Cappuccino, G. Cocorullo, P. Corsonello, and G. Schirinzi, "Design and demonstration of a real time processor for one-bit coded SAR signals," *IEE Proc.-Radar, Sonar Navigat.*, vol. 143, no. 4, pp. 261–267, Aug. 1996.

[23] V. Pascazio and G. Schirinzi, "Synthetic aperture radar imaging by one-bit coded signals," *Electron. Commun. Eng. J.*, vol. 10, no. 1, pp. 17–28, Feb. 1998.

[24] G. Fornaro, V. Pascazio, and G. Schirinzi, "Synthetic aperture radar interferometry using one bit coded raw and reference signals," *IEEE Trans. Geosci. Remote Sens.*, vol. 35, no. 5, pp. 1245–1253, Sep. 1997.

[25] G. Franceschetti, F. Impagnatiello, F. Rubertone, and M. Tesauro, "Results of the X-SAR real time one-bit processor," in *Proc. IEEE Int. Geosci. Remote Sens. Symp. (IGARSS)*, Honolulu, HI, USA, vol. 1, Jul. 2000, pp. 99–101.

[26] J. Yang, X. Huang, T. Jin, J. Thompson, and Z. Zhou, "Synthetic aperture radar imaging using stepped frequency waveform," *IEEE Trans. Geosci. Remote Sens.*, vol. 50, no. 5, pp. 2026–2036, May 2012.

[27] J. Yang, J. Thompson, X. Huang, T. Jin, and Z. Zhou, "Random-frequency SAR imaging based on compressed sensing," *IEEE Trans. Geosci. Remote Sens.*, vol. 51, no. 2, pp. 983–994, Feb. 2013.

[28] M. Wang, S. Yang, Z. Liu, and Z. Li, "Collaborative compressive radar imaging with saliency priors," *IEEE Trans. Geosci. Remote Sens.*, vol. 57, no. 3, pp. 1245–1255, Mar. 2019.

[29] S. Xing, S. Song, S. Quan, D. Sun, J. Wang, and Y. Li, "Near-field 3D sparse SAR direct imaging with irregular samples," *Remote Sens.*, vol. 14, no. 24, p. 6321, Dec. 2022.

[30] X. Dong and Y. Zhang, "A MAP approach for 1-Bit compressive sensing in synthetic aperture radar imaging," *IEEE Geosci. Remote Sens. Lett.*, vol. 12, no. 6, pp. 1237–1241, Jun. 2015.

[31] L. Jacques, J. N. Laska, P. T. Boufounos, and R. G. Baraniuk, "Robust 1-bit compressive sensing via binary stable embeddings of sparse vectors," *IEEE Trans. Inf. Theory*, vol. 59, no. 4, pp. 2082–2102, Apr. 2013.

[32] J. N. Laska, Z. Wen, W. Yin, and R. G. Baraniuk, "Trust, but verify: Fast and accurate signal recovery from 1-bit compressive measurements," *IEEE Trans. Signal Process.*, vol. 59, no. 11, pp. 5289–5301, Nov. 2011.

[33] M. Demir and E. Erçelebi, "One-bit compressive sensing with time-varying thresholds in synthetic aperture radar imaging," *IET Radar, Sonar Navigat.*, vol. 12, no. 12, pp. 1517–1526, Dec. 2018.

[34] Q. Fan, C. Jia, J. Liu, and Y. Luo, "Robust recovery in 1-bit compressive sensing via ℓ-constrained least squares," *Signal Process.*, vol. 179, Feb. 2021, Art. no. 107822.

[35] C. Stöckle, J. Munir, A. Mezghani, and J. A. Nossek, "1-bit direction of arrival estimation based on compressed sensing," in *Proc. IEEE 16th Int. Workshop Signal Process. Adv. Wireless Commun. (SPAWC)*, Jun. 2015, pp. 246–250.

[36] J. Han, G. Li, and X.-P. Zhang, "One-bit radar imaging via adaptive binary iterative hard thresholding," *IEEE Trans. Comput. Imag.*, vol. 7, pp. 1005–1017, 2021.

[37] J. Han, G. Li, K. Wang, M. Duan, and X.-P. Zhang, "1-bit radar imaging based on adversarial samples," *IEEE Trans. Geosci. Remote Sens.*, vol. 60, 2022, Art. no. 5101713.

[38] L. Wang, L. Zhao, G. Bi, C. Wan, and L. Yang, "Enhanced ISAR imaging by exploiting the continuity of the target scene," *IEEE Trans. Geosci. Remote Sens.*, vol. 52, no. 9, pp. 5736–5750, Sep. 2014.

[39] H. Duan, L. Zhang, J. Fang, L. Huang, and H. Li, "Pattern-coupled sparse Bayesian learning for inverse synthetic aperture radar imaging," *IEEE Signal Process. Lett.*, vol. 22, no. 11, pp. 1995–1999, Nov. 2015.

[40] Q. Wu, Y. D. Zhang, M. G. Amin, and B. Himed, "Complex multitask Bayesian compressive sensing," in *Proc. IEEE Int. Conf. Acoust., Speech Signal Process. (ICASSP)*, May 2014, pp. 3375–3379.

[41] S. Zhou, N. Xiu, and H.-D. Qi, "Global and quadratic convergence of Newton hard-thresholding pursuit," *J. Mach. Learn. Res.*, vol. 22, no. 1, pp. 599–643, 2021.

[42] R. Wang, N. Xiu, and C. Zhang, "Greedy projected gradient-Newton method for sparse logistic regression," *IEEE Trans. Neural Netw. Learn. Syst.*, vol. 31, no. 2, pp. 527–538, Feb. 2020.

[43] R. Wang, N. Xiu, and S. Zhou, "An extended Newton-type algorithm for $\ell 2$-regularized sparse logistic regression and its efficiency for classifying large-scale datasets," *J. Comput. Appl. Math.*, vol. 397, Dec. 2021, Art. no. 113656.

[44] L. Pan, S. Zhou, N. Xiu, and H.-D. Qi, "A convergent iterative hard thresholding for nonnegative sparsity optimization," *Pacific J. Optim.*, vol. 13, no. 2, pp. 325–353, 2017.

[45] M. Kim, Y. Song, S. Wang, Y. Xia, and X. Jiang, "Secure logistic regression based on homomorphic encryption: Design and evaluation," *JMIR Med. Informat.*, vol. 6, no. 2, p. e19, Apr. 2018.

[46] J. Fang, Y. Shen, H. Li, and Z. Ren, "Sparse signal recovery from one-bit quantized data: An iterative reweighted algorithm," *Signal Process.*, vol. 102, pp. 201–206, Sep. 2014.

[47] F. Li, J. Fang, H. Li, and L. Huang, "Robust one-bit Bayesian compressed sensing with sign-flip errors," *IEEE Signal Process. Lett.*, vol. 22, no. 7, pp. 857–861, Jul. 2015.

[48] P. J. G. Lisboa et al., "Partial logistic artificial neural network for competing risks regularized with automatic relevance determination," *IEEE Trans. Neural Netw.*, vol. 20, no. 9, pp. 1403–1416, Sep. 2009.

[49] P. A. Gutiérrez, C. Hervás-Martínez, and F. J. Martínez-Estudillo, "Logistic regression by means of evolutionary radial basis function neural networks," *IEEE Trans. Neural Netw.*, vol. 22, no. 2, pp. 246–263, Feb. 2011.

[50] C. M. Bishop and N. M. Nasrabadi, *Pattern Recognition and Machine Learning*, vol. 4, no. 4. Cham, Switzerland: Springer, 2006.

[51] M. Tan, I. W. Tsang, and L. Wang, "Minimax sparse logistic regression for very high-dimensional feature selection," *IEEE Trans. Neural Netw. Learn. Syst.*, vol. 24, no. 10, pp. 1609–1622, Oct. 2013.

[52] H. Zeng and A. Song, "Optimizing single-trial EEG classification by stationary matrix logistic regression in brain–computer interface," *IEEE Trans. Neural Netw. Learn. Syst.*, vol. 27, no. 11, pp. 2301–2313, Nov. 2016.

[53] Z. Qiu, D. J. Miller, and G. Kesidis, "A maximum entropy framework for semisupervised and active learning with unknown and label-scarce classes," *IEEE Trans. Neural Netw. Learn. Syst.*, vol. 28, no. 4, pp. 917–933, Apr. 2017.

[54] F. Liu, X. Huang, C. Gong, J. Yang, and J. A. K. Suykens, "Indefinite kernel logistic regression with concave-inexact-convex procedure," *IEEE Trans. Neural Netw. Learn. Syst.*, vol. 30, no. 3, pp. 765–776, Mar. 2019.

[55] H. Bi, G. Bi, B. Zhang, and W. Hong, "Complex-image-based sparse SAR imaging and its equivalence," *IEEE Trans. Geosci. Remote Sens.*, vol. 56, no. 9, pp. 5006–5014, Sep. 2018.

[56] S. Sun, G. Zhu, and T. Jin, "Novel methods to accelerate CS radar imaging by NUFFT," *IEEE Trans. Geosci. Remote Sens.*, vol. 53, no. 1, pp. 557–566, Jan. 2015.

[57] L. Greengard and J.-Y. Lee, "Accelerating the nonuniform fast Fourier transform," *SIAM Rev.*, vol. 46, no. 3, pp. 443–454, Jan. 2004.

[58] J. Fang, Z. Xu, B. Zhang, W. Hong, and Y. Wu, "Fast compressed sensing SAR imaging based on approximated observation," *IEEE J. Sel. Topics Appl. Earth Observ. Remote Sens.*, vol. 7, no. 1, pp. 352–363, Jan. 2013.

[59] X. Yang, G. Li, J. Sun, Y. Liu, and X.-G. Xia, "High-resolution and wide-swath SAR imaging via Poisson disk sampling and iterative shrinkage thresholding," *IEEE Trans. Geosci. Remote Sens.*, vol. 57, no. 7, pp. 4692–4704, Jul. 2019.

[60] H. Bi, B. Zhang, X. X. Zhu, W. Hong, J. Sun, and Y. Wu, "L_1-regularization-based SAR imaging and CFAR detection via complex approximated message passing," *IEEE Trans. Geosci. Remote Sens.*, vol. 55, no. 6, pp. 3426–3440, Jun. 2017.

[61] L. Kang, T. Sun, Y. Luo, J. Ni, and Q. Zhang, "SAR imaging based on deep unfolded network with approximated observation," *IEEE Trans. Geosci. Remote Sens.*, vol. 60, 2022, Art. no. 5228514.

[62] B. Li, F. Liu, C. Zhou, Z. Wang, and H. Han, "Mixed sparse representation for approximated observation-based compressed sensing radar imaging," *J. Appl. Remote Sens.*, vol. 12, no. 3, 2018, Art. no. 035015.

[63] L.-L. Pan, N.-H. Xiu, and S.-L. Zhou, "On solutions of sparsity constrained optimization," *J. Operations Res. Soc. China*, vol. 3, no. 4, pp. 421–439, Dec. 2015.

[64] M. Wang et al., "RMIST-net: Joint range migration and sparse reconstruction network for 3-D mmW imaging," *IEEE Trans. Geosci. Remote Sens.*, vol. 60, 2022, Art. no. 5205117.

[65] X. Meng and J. Zhu, "A generalized sparse Bayesian learning algorithm for 1-bit DOA estimation," *IEEE Commun. Lett.*, vol. 22, no. 7, pp. 1414–1417, Jul. 2018.

[66] X. Meng, S. Wu, and J. Zhu, "A unified Bayesian inference framework for generalized linear models," *IEEE Signal Process. Lett.*, vol. 25, no. 3, pp. 398–402, Mar. 2018.

[67] C. Jiang, B. Zhang, Z. Zhang, W. Hong, and Y. Wu, "Experimental results and analysis of sparse microwave imaging from spaceborne radar raw data," *Sci. China Inf. Sci.*, vol. 55, no. 8, pp. 1801–1815, Aug. 2012.

[68] S. Zhang, Y. Liu, and X. Li, "Fast entropy minimization based autofocusing technique for ISAR imaging," *IEEE Trans. Signal Process.*, vol. 63, no. 13, pp. 3425–3434, Jul. 2015.

Shaodi Ge received the M.S. degree from Beijing Forestry University, Beijing, China, in 2020. He is currently pursuing the Ph.D. degree with the National University of Defense Technology, Changsha, China.

His research interests include SAR imaging and array signal processing.

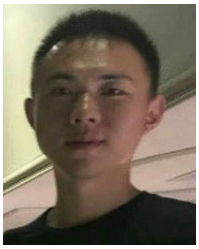

Dong Feng received the B.S. degree in information engineering and the M.S. and Ph.D. degrees in information and communication engineering from the National University of Defense Technology, Changsha, China, in 2013, 2015, and 2020, respectively.

He is currently a Lecturer with the National University of Defense Technology. His research interests include bistatic SAR image formation and holographic SAR 3-D image formation.

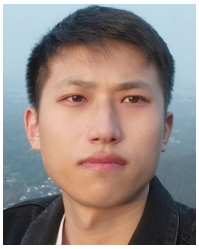

Shaoqiu Song received the B.S. degree from the Huazhong University of Science and Technology, Wuhan, China, in 2020. He is currently pursuing the Ph.D. degree with the National University of Defense Technology, Changsha, China.

His research interests include 3-D SAR imaging and MIMO signal processing.

Jian Wang received the B.S., M.S., and Ph.D. degrees in information and communications engineering from the National University of Defense Technology, Changsha, China, in 2003, 2004, and 2009, respectively.

He is currently an Associate Professor with the National University of Defense Technology. His research interests include ground surveillance radar, target tracking, SAR image formation, and SAR interferometry.

Xiaotao Huang (Member, IEEE) received the B.S. and Ph.D. degrees in information and communication engineering from the National University of Defense Technology, Changsha, China, in 1990 and 1999, respectively.

He is currently a Professor with the National University of Defense Technology. His research interests include radar theory, signal processing, and radio frequency signal suppression.